



TALLINN UNIVERSITY OF TECHNOLOGY  
SCHOOL OF ENGINEERING

Department of Electrical Power Engineering and Mechatronics

# DEVELOPMENT OF POWER CONDITIONING CONTROL STRATEGIES FOR FLYWHEEL STORAGE IN MICROGRID

HOORATAS-ENERGIASALVESTI JUHTIMISSTRATEEGIAATE ARENDAMINE  
MIKROVÕRGU TASAKAALUSTAMISEKS

## MASTER THESIS

Student:	Freddy Plaum
Student code:	176534 AAAM
Supervisor:	Tobias Häring
Co-supervisor:	Argo Rosin

Tallinn, 2019

(On the reverse side of title page)

## **AUTHOR'S DECLARATION**

Hereby I declare, that I have written this thesis independently.

No academic degree has been applied for based on this material. All works, major viewpoints and data of the other authors used in this thesis have been referenced.

"....." ..... 201.....

Author: .....

/signature /

Thesis is in accordance with terms and requirements

"....." ..... 201.....

Supervisor: .....

/signature/

Accepted for defence

"....." .....201... .

Chairman of theses defence commission: .....

/name and signature/

## ABSTRACT

*Author:* Freddy Plaum

*Type of the work:* Master Thesis

*Title:* Development of power conditioning control strategies for flywheel storage in microgrid

*Date:* May 2019

81 pages

*University:* Tallinn University of Technology

*School:* School of Engineering

*Department:* Department of Electrical Power Engineering and Mechatronics

*Supervisor(s) of the thesis:* Early Stage Researcher Tobias Häring, Professor Argo Rosin

*Consultant(s):* Early Stage Researcher Vahur Maask

*Abstract:*

The thesis consists of 81 pages, it contains 8 tables, 30 figures and 38 equations.

The goal of this thesis is to develop simplified models and control strategies for a flywheel energy storage system to improve power/voltage quality and stability in a microgrid with weak grid connection or in an islanded microgrid.

In the first part of this thesis an overview of the flywheel energy storage system is given. Comparison with other competing storage systems such as batteries and supercapacitors is drawn, explaining the position of flywheel system.

The second part of this thesis presents the development process of the flywheel storage model. It gives an overview of the modeled microgrid with the flywheel system, the consumer load and the grid connection. Development of field-oriented control of motor-side converter and current control of grid-side converter is also given in this part.

In the third part of the thesis multiple different on- and off-grid scenarios are simulated. Off-grid applications such as: use for uninterruptable power source and for grid synchronization are tested. On-grid active power load leveling and voltage regulation using reactive power are also simulated.

*Keywords:* flywheel energy storage, power conditioning, microgrid, nearly zero energy building, Matlab, Simulink

# LÕPUTÖÖ LÜHIKOKKUVÕTE

<i>Autor:</i> Freddy Plaum	<i>Lõputöö liik:</i> Magistritöö
<i>Töö pealkiri:</i> Hooratas-energiasalvesti juhtimisstrateegiate arendamine mikrovõrgu tasakaalustamiseks	
<i>Kuupäev:</i> Mai 2019	81 lk
<i>Ülikool:</i> Tallinna Tehnikaülikool	
<i>Teaduskond:</i> Inseneriteaduskond	
<i>Instituut:</i> Elektroenergeetika ja mehhatroonika instituut	
<i>Töö juhendaja(d):</i> doktorant-nooremteadur Tobia Häring, professor Argo Rosin	
<i>Töö konsultant (konsultandid):</i> doktorant-nooremteadur Vahur Maask	
<i>Sisu kirjeldus:</i> <p>Lõputöö koosneb 81 lehest ning sisaldab 8 tabelit, 30 joonist ning 38 võrrandit.</p> <p>Käesoleva lõputöö eesmärgiks on arendada lihtsusatud mudelid ja juhtimisstrateegiad hooratas-energiasalvesti kasutuseks võimsuse ja pingekvaliteedi parendamiseks nõrga ühendusega mikrovõrgus või võrguühenduseta mikrovõrgus.</p> <p>Töö esimeses osas antakse ülevaade hooratas-energiasalvestist. Tuuakse võrdlus konkureerivate salvestusseadmetega, mille põhjal kirjeldatakse hooratas-energiasalvesti otstarvet.</p> <p>Töö teises osas kirjeldatakse hooratas-energiasalvesti mudelite arendamise protsessi. Antakse ülevaade mikrovõrgu mudeli komponentidest nagu hooratas-energiasalvestit, tarbijatest ja võrguühendusest. Mootori- ja võrgupoolsete muundurite juhtimisalgoritmide arendus on samuti toodud selles osas.</p> <p>Töö kolmandas osas simuleeritakse mitmeid erinevaid võrguühendusega ja -ühenduseta stsenaariume. Võrguühenduseta stsenaariumitest testitakse katkematu toiteallika ja võrgu sünkroniseerimise kasutust. Võrguühendusega stsenaariumitest testitakse aktiivvõimsuslike koormuste tasandamist ja võrgupinge reguleerimist reaktiivvõimsust kasutades.</p>	
<i>Märksõnad:</i> hooratas-energiasalvesti, võimsuskvaliteedi parendamine ,mikrovõrk, liginullenergiahoone, Matlab, Simulink	

# THESIS TASK

Thesis title: **Development of power conditioning control strategies for flywheel storage in microgrid**  
**Hooratas-energiasalvesti juhtimisstrateegiate arendamine mikrovõrgu tasakaalustamiseks**

Student: **Freddy Plaum, 176534 AAAM**

Programme: **Energy Conversion and Control Systems**

Type of the work: **Master Thesis**

Supervisor of the thesis: **Tobias Häring, Argo Rosin**

Validity period of the thesis task: **23.06.2019**

Submission deadline of the thesis: **24.05.2019**

---

Student (signature)

---

Supervisor (signature)

---

Head of programme (signature)

## 1. Reasons for choosing the topic

As nations around the world are moving to adopt green environmental policies that have led to the rise in the use of renewable energy sources, the research into balancing the production and consumption has become another important topic. This increase of renewable energy sources can lead to power supply reliability issues in the future. A result of this can be temporary islanded operation of microgrids. Different demand side management and load scheduling methods influence the stability and power/voltage quality of such a microgrid. This thesis will contribute to the existing work in the field by investigating the use of a flywheel energy storage system in a microgrid context.

## 2. Thesis objective

The aim of this thesis is to develop simplified mathematical models and control strategies for a flywheel energy storage system to improve power/voltage quality and stability in a microgrid with weak grid connection resp. an islanded microgrid.

## 3. List of sub-questions:

Is the reaction time of the flywheel energy storage system model sufficient for power conditioning?

How viable is the use of a flywheel energy storage system for power production and consumption balancing?

How capable is the flywheel system in voltage regulation through reactive power compensation?

#### **4. Basic data:**

Datasheets of the laboratory flywheel energy storage components, from supervisors.

Data on the characteristics and properties of flywheel energy storage systems, from literature.

Data from the results of the Matlab/Simulink simulations.

#### **5. Research methods**

The research in this work is conducted based on the analysis of literature and modeling of Matlab simulations.

Matlab/Simulink models are developed based on literature analysis and datasheets. The models of the components are then validated with simple test signals. Finally, scenarios are implemented to simulate the research objectives with the developed models. The data analysis will be done in Matlab/Simulink.

#### **6. Graphical material**

Graphical materials include explanatory drawings, schematics, tables or diagrams, and matlab simulation results, they are part of the main work.

#### **7. Thesis structure**

Introduction

##### 1. State of the Art

###### 1.1 Flywheel energy storage system

###### 1.1.1 Components of FESS

###### 1.1.2 Applications of FESS

###### 1.1.3 Comparison to other storage technologies

###### 1.2 Microgrids

##### 2. Development of FESS model

###### 2.1 Modeled physical components

###### 2.1.1 Flywheel system model

###### 2.1.2 Grid and consumer model

###### 2.2 Converter control strategies

###### 2.2.1 FESS control unit

###### 2.2.2 Speed controller

- 2.2.3 Clarke and Park transforms
- 2.2.4 Space vector modulation
- 2.2.5 Field oriented control of motor-side converter
- 2.2.6 Current control of grid-side converter

### 3. Simulations

- 3.1 Off-Grid scenarios
  - 3.1.1 Islanding / UPS
  - 3.1.2 Grid synchronication
- 3.2 On-Grid scenarios
  - 3.2.1 Voltage regulation using reactive power
  - 3.2.2 Load leveling using active power

Summary

## 8. References

Sources used in this work come from books, research articles, standards, ect. Some of the sources used are listed below.

Q.-C. Zhong and T. Hornik, Control of Power Inverters in Renewable Energy and Smart Grid Integration, Wiley-IEEE Press, 2013.

M. E. Amiryar and K. R. Pullen, "A Review of Flywheel Energy Storage System," *Applied Sciences*, vol. 7, no. 3, p. 286, 2017.

P. Nikolaidis and A. Poullikkas, "A comparative review of electrical energy storage systems for better sustainability," *Journal of Power Technologies*, vol. 97, no. 3, pp. 220-245, 2018.

P. Yulong, A. Cavagnino, V. Silvio, C. Feng and A. Tenconi, "Flywheel energy storage systems for power systems application," in *ICCEP*, Santa Margherita Ligure, 2017.

## 9. Thesis consultants

Vahur Maask

## 10. Work stages and schedule

- 23. December – Going through the literature
- 21. January – Writing the theoretical part
- 25. February – Matlab FESS model
- 22. March – Matlab simulation scenarios
- 29. April – Writing the modeling part
- 20. May – Completing the final version of the thesis

# CONTENTS

PREFACE .....	11
LIST OF ABBREVIATIONS AND SYMBOLS USED .....	12
INTRODUCTION .....	14
1. FLYWHEEL ENERGY STORAGE SYSTEM.....	16
1.1 Components of FESS.....	16
1.1.1 Flywheel-Rotor .....	17
1.1.2 Motor-Generator unit .....	19
1.1.3 Bearings.....	20
1.1.4 Containment housing .....	21
1.1.5 Power Electronics.....	22
1.2 Comparison to other energy storage systems .....	23
1.3 Applications of FESS .....	25
1.3.1 Grid stability improvement .....	25
1.3.2 Uninterruptible power supply .....	26
1.3.3 Renewable integration .....	26
1.4 Microgrids and nearly zero energy buildings .....	27
2. DEVELOPMENT OF FESS MODEL .....	29
2.1 Modeled physical components .....	29
2.1.1 Flywheel system .....	29
2.1.2 Grid model description.....	33
2.2 Converter control strategies .....	34
2.2.1 FESS control unit .....	35
2.2.2 Speed controller .....	40
2.2.3 Clarke and Park transforms .....	42
2.2.4 Field oriented control of motor-side converter .....	43
2.2.5 Space Vector Modulation.....	46
2.2.6 Current control of grid-side converter .....	48
3. SIMULATIONS .....	52
3.1 OFF-Grid Scenarios.....	52
3.1.1 Islanding / UPS.....	52
3.1.2 Grid synchronization .....	55
3.2 ON-Grid Scenarios .....	56
3.2.1 Voltage regulation using reactive power .....	56
3.2.2 Load leveling using active power .....	57

SUMMARY .....	61
KOKKUVÕTE .....	63
REFERENCES .....	65
APPENDICES .....	69
Appendix 1 Matlab code used for flywheel system modeling .....	70
Appendix 2 Simulink model of physical components .....	72
Appendix 3 Simulink model of variable load block .....	73
Appendix 4 Simulink model of FESS control.....	74
Appendix 5 Simulink model of state selection logic.....	75
Appendix 6 Simulink model of startup mode.....	76
Appendix 7 Simulink model of motorin/regen mode .....	77
Appendix 8 Simulink model of standby mode .....	78
Appendix 9 Simulink model of Speed Controller .....	79
Appendix 10 Simulink model of Field-Oriented Control of MSC.....	80
Appendix 11 Simulink model of Current Control of GSC.....	81

## **APPLICATION IN ENGLISH**

23.05.2019

From: Freddy Plaum (176534AAAM)

To: Ivo Palu

Application

I, Freddy Plaum, would like to request the permission to write this master thesis in English because the supervisor of this thesis is from Germany and his Estonian skill is not good enough to properly evaluate works written in Estonian.

Thank you for your understanding.

Freddy Plaum

## **PREFACE**

This thesis was derived from the research of PhD students Tobias Häring into microgrids and nearly zero energy buildings.

This thesis topic was provided to me by my supervisors, early stage researcher Tobias Häring and professor Argo Rosin, to whom I would like to extend my gratitude for their continuous support and guidance throughout the whole work.

I would like to thank Vahur Maask and rest of the members of the Microgrids and Metrology research group who provided valuable consultation for this work.

I would like to give my special thanks to my family for their constant support during my pursuit of higher education.

Freddy Plaum

## LIST OF ABBREVIATIONS AND SYMBOLS USED

AMB	Active Magnetic Bearings
CAES	Compressed Air Energy Storage
DER	Distributed Energy Resources
DG	Distributed Generation
DSM	Demand Side Management
DSO	Distribution System Operator
ESS	Energy Storage System
EU	European Union
FCU	FESS Control Unit
FES	Flywheel Energy Storage
FESS	Flywheel Energy Storage System
FOC	Field-Oriented Control
GSC	Grid Side Converter
IFOC	Indirect Field-Oriented Control
IM	Induction Motor
MSC	Motor Side Converter
nZEB	Nearly Zero Energy Building
PCC	Point of Common Coupling
PHS	Pumped Hydro Storage
PI	Proportional-Integral
PLL	Phase Locked Loop
PMB	Passive Magnetic Bearings
PV	Photovoltaic
PWM	Pulse Width Modulation
RMS	Root Mean Square

RMSE	Root Mean Squared Error
SMB	Superconducting Magnetic Bearings
SMES	Super-conducting magnetic energy storage
SPWV	Sinusoidal Pulse Width Modulation
SVM	Space Vector Modulation
THD	Total Harmonic Distortion
UPS	Uninterruptable Power Source
V/Hz	Voltage / Frequency
ZEBRA	Zero Emissions Batteries Research Activity

## INTRODUCTION

Due to rising concerns about global warming and unsustainability of conventional fossil fuel energy sources, many nations around the world have adopted environmental policies that have led to a rise in production of green renewable energies, such as solar or wind. In 2009 the European Union (EU) set a goal that by 2020 at least 20% of EUs energy needs must be met through renewables [1].

This trend can be seen worldwide as the global investments into renewable energies has risen from 61,7 billion (10<sup>9</sup>) USD in 2004 to 333,5 billion USD in 2017 [2]. In Estonia the renewable energy usage has increased 12,7% in ten years, from 16,1% in 2006 to 28,8% in 2016 [2].

Another trend seen is the change of paradigm from employment of few large-scale power plants to a more distributed generation (DG) that brings production closer to the end-user. This can be observed from the development of microgrids and nearly zero energy buildings (nZEB). Both microgrids and nZEB utilize some form of on-site generation to either supply power during an islanded operation or to reach nearly zero energy balance.

The EU has set out directive that requires all new buildings to be nZEB by the end of 2020 [3]. Many of these nZEB use solar panels to produce during the day when home power consumption is low. It logically follows that the energy generated needs to either be sold to the distribution system operator (DSO) or to be saved for later use.

Grid-connected nZEB could be considered as microproducers. In Estonia microproducers are defined as small producers whose power output is less than 15 kW [2]. The number of microproducers in Estonia increased from 0 in 2011 to 1045 by 2017 [2]. This sharp increase was seen due to subsidizations for small-scale green energy installments that begun in 2012 [4].

Increased movement towards the use of renewable energies in DG has resulted in an additional source of fragility in power grids. The unbalance of production and consumption can introduce deviations in grid parameters such as voltage and frequency. Balancing power systems with many distributed renewable sources can prove to be difficult due to sources such as solar and wind being inherently unpredictable and fluctuating.

Energy storage systems (ESS) can be used for balancing to store overproduced energy for later use when needed. It can be differentiated between long term and short term balancing needs.

Long term balancing is needed to level out daily power production and consumption peaks. This type of imbalance can be decreased with use of large-scale long-term storage systems with low running losses, such as pumped hydro storage (PHS) or compressed air energy storage (CAES).

Another option would be to shift consumption through methods like demands side management (DSM).

Short term balancing needs however stem from quick fluctuations in production of renewables or consumption due to turn on of large loads. Short term balancing can be performed with quickly reacting small-scale ESS such as batteries, supercapacitors or flywheel energy storage systems (FESS).

Flywheels have been used as means of energy storage for thousands of years, they were one of the first mechanical energy storage systems ever invented. They were used in potter's wheel, water wheels, hand mills and other cyclic rotating mechanical systems to add inertia for smoother operations. Flywheels saw large scale use after the beginning of the industrial revolution. These days' flywheels are still used in a large variety of different industries and seen as a potentially viable option for energy storage systems [5].

The aim of this thesis is to develop simplified models and control strategies for a flywheel energy storage system to improve power/voltage quality and stability in a microgrid with weak grid connection resp. an islanded microgrid.

Four simulation scenarios were considered that can be broadly classified as off-grid and on-grid scenarios. On-grid scenarios such as active power load leveling and voltage regulation through reactive power were modeled. For off-grid the use of FESS for islanding / uninterruptable power source (UPS) and grid synchronization were also considered.

The models for FESS were created based on the parameters of 15 kW Rosetta T3-15 flywheel system located in Tallinn University of Technology. Its control mechanisms and power conditioning scenarios were simulated in MATLAB/Simulink environment. Chapter 1 of this thesis gives an overview of FESS, its components, compares it to other competing energy storage systems and suitable applications. Chapter 2 describes the development process of FESS model, what control algorithms were used and their verification. In Chapter 3 different on- and off-grid scenarios were simulated.

# 1. FLYWHEEL ENERGY STORAGE SYSTEM

Flywheel based energy storage systems store energy in a rotating mass as a kinetic energy. The flywheel energy storage (FES) systems discussed in this thesis are electromechanical devices that convert between electric and kinetic energy using a machine that is able to work as a motor and generator. Energy is transferred either by accelerating or decelerating the flywheel.

## 1.1 Components of FESS

Flywheel energy storage systems are composed of a chamber enclosed motor-generator unit that is connected to a flywheel mass with a shaft that sits on bearings. The energy drawn or stored in the flywheel is controlled through power electronics components connected between the motor-generator and the grid [6]. The construction of a high-speed FES system is depicted in Figure 1.1.

FES systems can be classified broadly into two categories: low-speed FESS, with a rotating speed up to 10000 rpm and high-speed FESS, with a rotating speed up to 100000 rpm. Low-speed FESS typically have a heavy steel flywheel that rotates on mechanical bearings in non-vacuum chamber. That type of flywheel systems has low energy storage capabilities and high losses, but lower cost than high-speed systems. High-speed FESS usually have a lightweight composite material flywheel that rotates in high speed on magnetic bearings in a vacuum enclosure. This type of flywheel systems have high energy storage capabilities and low losses, however, they are more costly compared to low-speed systems [5].

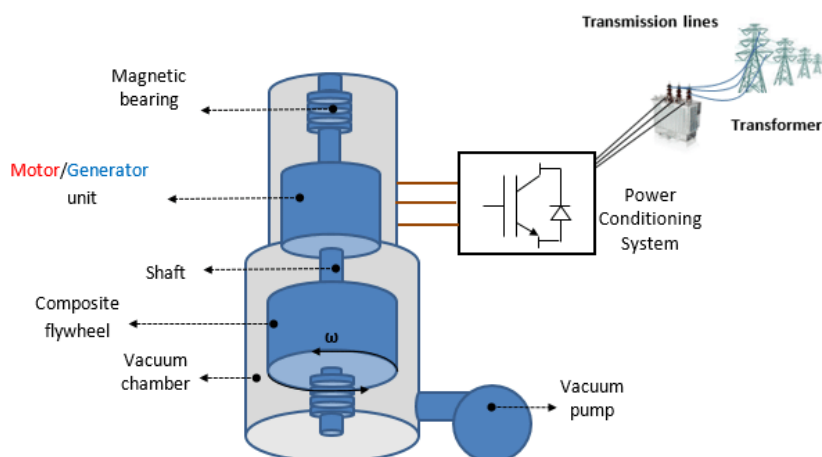


Figure 1.1 Construction of high-speed FESS [6]

### 1.1.1 Flywheel-Rotor

The energy stored in a flywheel is determined by the inertia of the flywheel and its rotational speed. According to equation 1.1 the stored energy scales linearly with the inertia of the flywheel and by the square of the rotational speed [5]. Therefore, lightweight high-speed flywheel systems can store more energy.

$$E_k = \frac{1}{2} I \omega^2 \quad (1.1)$$

where  $E_k$  – stored kinetic energy, J = Ws,

$I$  – inertia of the flywheel, kgm<sup>2</sup>,

$\omega$  – rotational speed of the flywheel, rad/s.

Commercially used flywheel systems usually operate within some minimum and maximum speed values, the energy stored in that range can be calculated with equation 1.2 [5].

$$E_k = \frac{1}{2} I (\omega_{\max}^2 - \omega_{\min}^2) \quad (1.2)$$

The moment of inertia is determined by the shape and mass of the flywheel and can be derived with equation 1.3 [7].

$$I = \int r^2 dm \quad (1.3)$$

where  $r$  – distance of each mass element from the central spinning axis, m,

$dm$  – differential mass element.

The moment of inertia of a solid cylindrical flywheel can be expressed with equation 1.4 [5].

$$I = \frac{1}{2} m r^2 \quad (1.4)$$

where  $m$  – mass of the flywheel, kg,

$r$  – radius of the flywheel, m.

The centrifugal forces affecting the flywheel determine the maximum speed it can rotate at and therefore also the maximum energy it can store. The energy density  $e_v$  and specific energy  $e_m$ , referring to the volume and mass of the flywheel respectively, are given with equations 1.5 and 1.6 [7].

$$e_v = K \quad (1.5)$$

$$e_m = K \frac{\sigma}{\rho} \quad (1.6)$$

where  $K$  – shape factor of the flywheel,

$\sigma$  – tensile strength of the flywheel material, Pa,

$\rho$  – mass density of the flywheel material, kg/m<sup>3</sup>.

The shape factor  $K$  is a constant derived from the shape of the rotor, figure 1.2 shows some of the possible flywheel shapes with their shape factors.

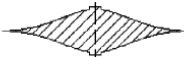
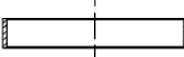
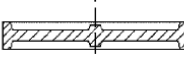
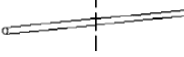
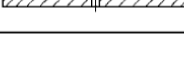
Fly wheel geometry	Cross section	Shape factor K
Disc		1.000
Modified constant stress disc		0.931
Conical disc		0.806
Flat unpierced disc		0.606
Thin firm		0.500
Shaped bar		0.500
Rim with web		0.400
Single bar		0.333
Flat pierced bar		0.305

Figure 1.2 Shape factor K for different flywheel shapes [8]

Characteristics of some of the metal and composite flywheel materials commonly used in low- and high-speed flywheels are shown in table 1.1, from which it can be deduced that the materials that have low mass density and high tensile strength can store the most energy.

Table 1.1 Characteristics of commonly used flywheel materials [7]

Material	$\rho$ [kg/m <sup>3</sup> ]	$\sigma_{\theta,u}$ [MPa]	$e_v$ [MJ/m <sup>3</sup> ]	$e_m$ [kJ/kg]
Aluminium	2700	500	251	93
Steel	7800	800	399	51
Glass E/Epoxy	2000	1000	500	250
Graphite HM/Epoxy	1580	750	374	237
Graphite HS/Epoxy	1600	1500	752	470

### 1.1.2 Motor-Generator unit

In order to realize electromechanical conversion between electric and kinetic energies, an electrical machine capable of operating both, as an electric motor and an electric generator, is used. When the flywheel is being charged, the machine is operating as a motor, accelerating the flywheel. The stored energy is later extracted by slowing down the flywheel, while the machine is operating as a generator [5]. Table 1.2 compares commonly used electrical machines in flywheel energy storage systems: asynchronous induction machines, permanent magnet machines and variable reluctance machines.

Table 1.2 Comparison of commonly used electrical machines used in FES systems [5]

Machine	Asynchronous Induction	Variable Reluctance	Permanent Magnet Synchronous
Power	High	Medium and low	Medium and low
Specific power	Medium ( $\approx 0,7$ kW/kg)	Medium ( $\approx 0,7$ kW/kg)	High ( $\approx 1,2$ kW/kg)
Rotor losses	Copper and iron	Iron due to slots	Very low
Spinning losses	Removable by annulling flux	Removable by annulling flux	Non-removable, static flux
Efficiency	High (93,4 %)	High (93 %)	Very high (95,5 %)
Control	Vector control	Synchronous: Vector Switched: DSP	Sinusoidal: Vector Trapezoidal: DSP
Size	1,8 L/kW	2,6 L/kW	2,3 L/kW
Torque ripple	Medium (7,3 %)	High (24 %)	Medium (10 %)
Maximum/base speed	Medium ( $> 3$ )	High ( $> 4$ )	Low ( $< 2$ )
Cost	Low (22 €/kW)	Low (24 €/kW)	Low (38 €/kW)

The advantages of using an induction motor are that it is well suited for high power and high torque applications and it has low running losses. However, it requires complex control systems and more maintenance. A variable reluctance motor has an advantage of wide speed range and its control is simpler than that of an induction motor. Nevertheless, it has a low power factor, low power density

and a high torque ripple. The advantages of permanent magnet machines are their high efficiency, high power density and low rotor losses. However, they have idling losses due to permanent magnet induced eddy current losses. The most commonly used machines for FESS applications are permanent magnet machines. They are used widely due to limitations of other machines, such as speed, torque limitations and control difficulties [5].

### 1.1.3 Bearings

Bearings are used to support flywheel shaft both radially and axially. The choice of the type of bearings to use in flywheel system is important, because it determines the running friction losses and the maximum speed that the flywheel is capable of rotating at. The most commonly used bearings in flywheel systems are mechanical bearings, magnetic bearings and hybrid bearings [9].

Traditional mechanical bearings are well proven in many different industries. They are inexpensive, take up small amount of space and are used in cheap, low-speed flywheel systems. They are not very suitable for high-speed flywheels due to high friction losses, wear and tear, and lubrication degradation or evaporation in vacuum [9].

Magnetic bearings work by levitating the rotor shaft with magnetic fields. This type of bearings are contactless, meaning they provide low losses, long lifetime and do not need lubrication. There are multiple types of magnetic bearings: passive (PMB), active (AMB) and superconducting magnetic bearings (SMB). PMB use permanent magnets, while AMB use current passing coils to generate magnetic fields. SMB are more expensive and require cryogenic cooling to cool down the high temperature superconductors. Magnetic bearings are well suited for high-speed flywheel systems [9]. Figure 1.3 shows a cross-sectional comparison between bearings used in a low- and high-speed flywheels.

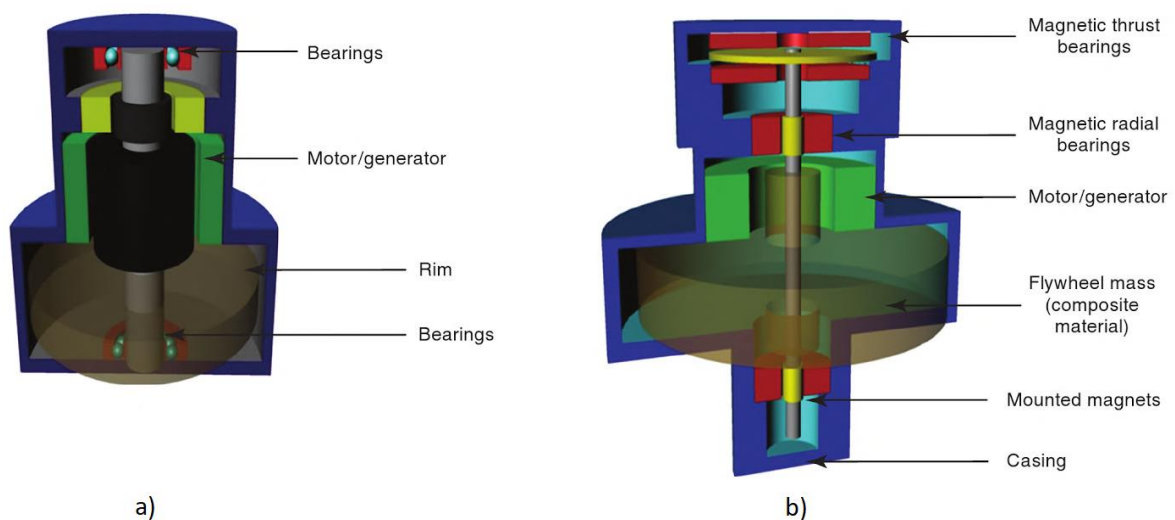


Figure 1.3 Bearing comparison between a low-speed flywheel (a) and a high-speed flywheel (b) [10]

In practice hybrid bearings are often used in flywheel systems as a price and performance compromise. In a vertically aligned flywheel systems it is important to support the gravitational load of the flywheel and to hold the rotating flywheel in place. These functions are often split between two different types of bearings [9].

### 1.1.4 Containment housing

Commercially sold flywheel systems are contained in a housing for safety reasons as a catastrophic failure of even low-speed flywheels can be very dangerous due to the large masses and therefore forces involved. Flywheels made of composite materials tend to fragment into pieces in the event of failure and there is a possibility of a dust explosion in case air should enter the closure [5].

In high speed models the inside of the chamber is sometimes pumped into vacuum to reduce the atmospheric friction, otherwise the aerodynamic drag loss increases with the cube of the rotational speed in a standard atmospheric pressure. Low pressure operation requires additional cooling systems to cope with the heat losses of other parts such as motor-generator unit. The housing is usually made of thick steel and can contribute to half of the flywheel systems weight [5]. Various different flywheel component configurations are shown in figure 1.4.

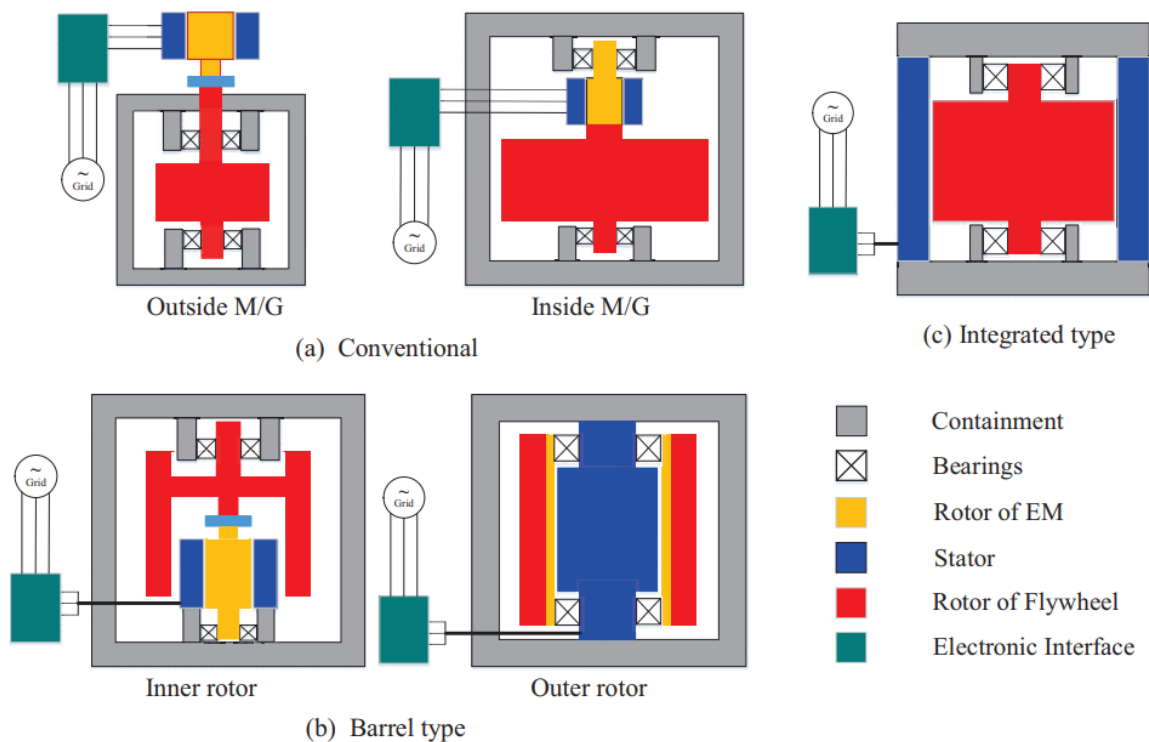


Figure 1.4 Various different flywheel system configurations: a) conventional type, b) barrel type, c) integrated type [9]

### 1.1.5 Power Electronics

Power electronics components are used to connect the FES system to the grid to direct the power flow between FESS and the grid. The most commonly used configuration composes of two bidirectional AC-DC converters connected back-to-back with a dc link capacitor in between them. When multiple flywheels are used, they can be connected to share a common dc bus [11], as shown in figure 1.5.

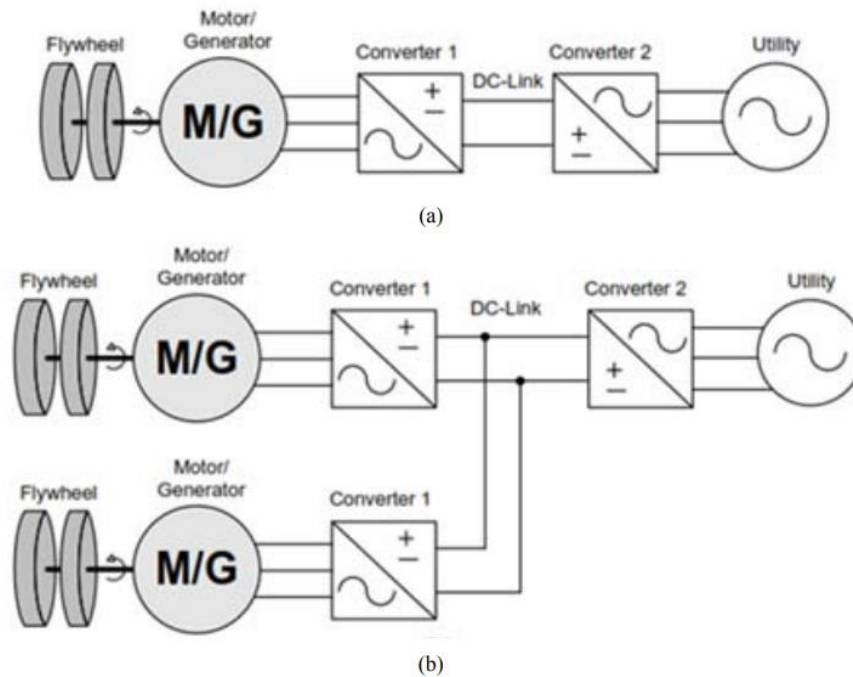


Figure 1.5 Different flywheel converter configurations: a) single flywheel system, b) multiple flywheel system [11]

The converters used in a FESS have to be bidirectional due to the different power flow directions during the charging and discharging modes. While charging, the FES system is drawing power from the grid: The grid side converter (GSC) works as an inverter and the motor side converter (MSC) as a rectifier. During the discharging mode, the inverting and rectifying operations are reversed [11].

The charging and discharging modes are determined by the power command set for the GSC control, which directs the power flow between DC-link and the grid. As a result, the DC-link voltage either rises or falls. The MSC is therefore controlled to maintain the DC-link voltage by directing the power flow between the DC-link and the motor/generator unit either by accelerating or decelerating the flywheel [7].

## 1.2 Comparison to other energy storage systems

Energy storage systems (ESS) considered in this chapter are systems where energy is stored in a state corresponding to the technology used and can be converted back to electricity when necessary. Commercially popular ESS can be classified into four categories by the state of stored energy [12]:

**Mechanical energy** storages include pumped hydro storages (PHS), compressed air energy storages (CAES) and flywheel energy storages (FES). These can store energy in a form that can later be used to drive a generator. A PHS stores energy by pumping water into higher level while a CAES stores energy by compressing air. Both PHS and CAES release energy by running a turbine that drives a generator. As discussed earlier a FES stores energy by spinning up a weight that can be used later to run a generator [12].

**Electrical energy** can be stored by using supercapacitors and super-conducting magnetic energy storage (SMES). Supercapacitors store energy in the electric field between two electrodes. Modern electrolyte and layering technologies can increase the stored energy of supercapacitors to make them a competitive choice for certain applications. SMES store energy in a strong magnetic field of a coil that is cooled down to become superconducting [12].

**Thermal energy** storage technologies can be divided into high and low temperature thermal energy storage systems. In high temperature systems the energy is stored by heating up material like magnesium oxide or molten salt. To release the stored energy, water is turned into steam and used to drive a turbine generator. Low temperature systems are kept below freezing temperature and used for cooling [12].

**Chemical energy** storage encompasses various battery storage technologies such as lithium-ion batteries, flow batteries, lead-acid batteries, high temperature (ZEBRA) batteries and hydrogen fuel cells. As the name states, chemical energy storage devices charge and discharge through chemical reactions like ion-exchange or oxidization [12].

There is a wide variety of different ESS with different characteristics that make it difficult to assess which one is the best for an application. It is always a compromise between different requirements for the needed storage system. Energy storage systems are compared by their power rating and energy capacity in figure 1.6. A comparison between flywheel storage and commercially competing battery and supercapacitor storage is shown in table 1.3. Flywheel systems are not in direct competition with PHS or CAES as those are large scale, high power and high energy storage systems that require large infrastructure to accommodate for them.

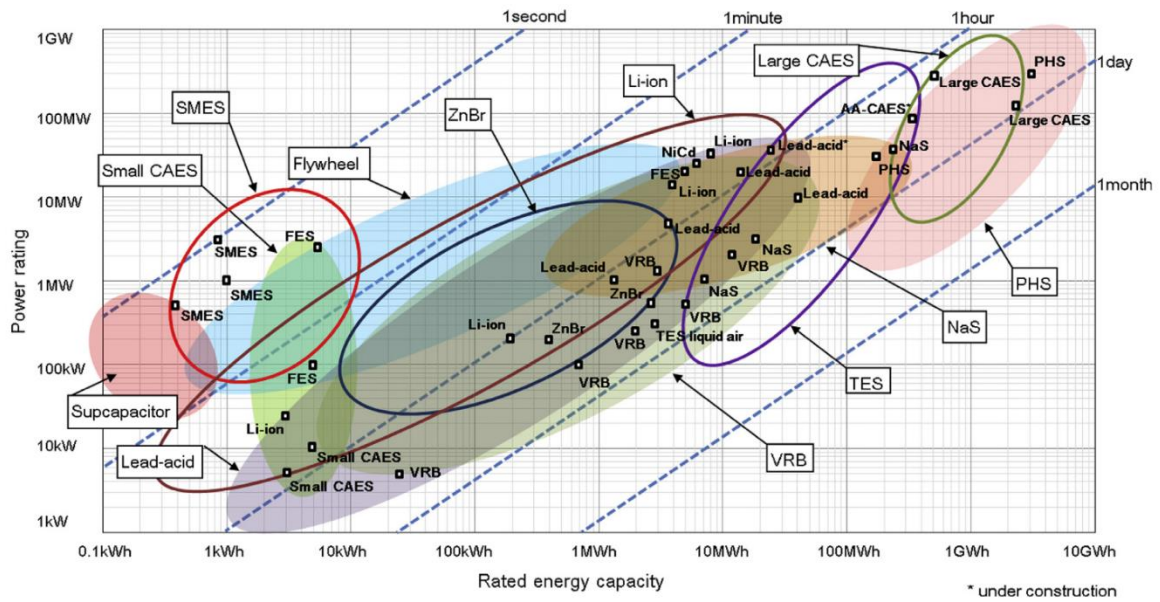


Figure 1.6 Energy storage technologies by their power rating and rated energy capacity [12]

Table 1.3 Comparison of different energy storage technologies [12]

Parameter	Supercapacitor	FES	Li-ion	Lead-Acid	ZEBRA
$\eta$ [%]	90-94	80-95	83-86	75-80	75-80
$E_v$ [Wh/l]	2-10	80-200	200-350	50-100	150-250
$E_m$ [Wh/kg]	2,5-15	5-80	75-250	30-50	100-140
$P_v$ [W/l]	15000	10000	100-3500	10-500	n.a.
$N_{cyc}$	Millions	Millions	1000-5000	500-2000	5000-10000
$L_{ca}$ [y]	15	15	5-20	5-15	15-20
$S_d$	10-15[%/h]	5-15[%/h]	0,1-0,2[%/day]	0,1-0,4[%/day]	10[%/day]
$C_p$ [€/kW]	10-20	300	150-200	150-200	150-200
$C_e$ [€/kWh]	10000-20000	1000	300-800	100-250	500-700

The description of the parameters used for comparison in table 1.3 are as follows [12]:  $\eta$ [%] – round-trip efficiency,  $E_v$ [Wh/l] – energy density,  $E_m$ [Wh/kg] – specific energy,  $P_v$ [W/l] – power density,  $N_{cyc}$  – lifetime charge cycles,  $L_{ca}$ [y] – calendar lifetime,  $S_d$  – self discharge,  $C_p$ [€/kW] – power installation cost,  $C_e$ [€/kWh] – energy installation cost.

Table 1.3 and figure 1.6 show that Li-ion and lead-acid based battery systems excel at long term storage due to their high storage capacitance and low self-discharge. However, they have low number of charge and discharge cycles and lack in power density, meaning they require more space for high power applications.

Supercapacitors on the other hand have high power density and can be used for millions of charge cycles, but the lack severely in energy storage capacity, meaning they are only reasonable for short term, high power applications.

Flywheel systems are in the middle ground by having relatively high power, storage and charge cycles. Nevertheless, their high self-discharge makes their use for long term energy storage suboptimal. These characteristics make flywheel systems suitable for high power, cyclic applications that still require sizable amount of energy to be exchanged with the grid.

### 1.3 Applications of FESS

Flywheel energy storage systems can be used in various applications that range from small scale consumer systems to large scale grid applications. Flywheels find their best use in applications that require high power for short durations in a cyclic nature. Therefore, FESS is most commonly used for power quality applications like voltage and frequency regulation or as an uninterruptable power source (UPS) and for load leveling. Large scale energy storage applications can also be achieved by arranging many high capacity, high-speed flywheels in banks [5]. The advantages and disadvantages of FESS compared to competing systems are shown in table 1.4.

Table 1.4 Pros and cons of flywheel energy storage systems [8], [13], [14]

Advantages	Disadvantages
High power density	Low energy capacity
High energy density (high-speed flywheels)	Low energy density (low-speed flywheels)
No capacity degradation over time	High self-discharge
Many charge cycles (over $10^5$ )	High investment cost
Short recharge time	
Easily estimated state-of-charge.	
Low running cost	
Environmentally friendly	
Scalable technology	

#### 1.3.1 Grid stability improvement

To provide a safe and reliable operation of the power grid, it is necessary to maintain the system voltage and frequency within acceptable levels. Unbalance between power consumers and producers lead to instabilities in voltage and frequency. Regulating voltage and frequency requires using fast-acting energy storage systems that can quickly either consume or provide power to grid. These regulation services are also very cyclic in their nature, meaning that the used energy storage system will rarely be resting. Traditional battery storage systems have limited charge-discharge cycles and their capacity degrades with use as mentioned in chapter 1.2. However, flywheels can

provide high power in short durations while retaining practically unlimited charge-discharge cycles without degrading in capacity [5].

### 1.3.2 Uninterruptible power supply

During power emergency situations it is necessary to maintain power in crucial locations like hospitals and safety systems like fire protection and evacuation. To provide uninterruptible power supply it is needed to use instantaneously reacting energy storage systems. Battery storage is currently widely used in UPS applications; however, flywheel storage is starting to be seen as a potential alternative due to its longer lifetime. Using flywheel storage in combination with battery storage or diesel generators is seen as an economical compromise for longer power outages. Flywheels can be used to bridge the gap between power loss and startup of diesel generators or to reduce charge-discharge cycles on the batteries from short term power losses [5].

### 1.3.3 Renewable integration

As nations around the world are moving away from environmentally unfriendly fossil fuels by increasing their renewable energy usage, a new source of fragility has appeared in power grid. These renewable energy sources such as wind and solar are unpredictable and fluctuating in their nature while also being usually produced by many smaller distributed generators in a decentralized manner. This increase in renewable energy can then lead to power supply reliability issues. As such, balancing the production of these renewable energy sources has become an important topic. Energy storage systems are thus looked into as means for power leveling [15]. Figure 1.7 shows an example of power generation smoothing for wind power generation where a flywheel system charged during excess generation and discharged when needed.

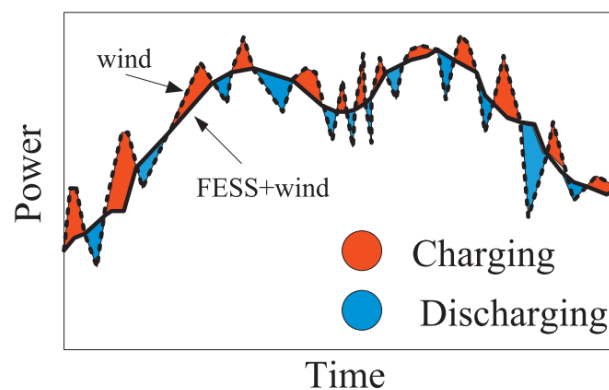


Figure 1.7 Wind power generation with and without FESS [15]

## 1.4 Microgrids and nearly zero energy buildings

Due to an ever-increasing electricity demand, more and more of the world's energy industries are looking for ways to save energy and to manage the ever-growing electrical grid. One solution that has been investigated is splitting up the grid into smaller microgrids that could be managed independently if needed [16].

The definition of a microgrid has not been unanimously agreed upon, but the US Department of Energy has defined a microgrid as “a group of interconnected loads and distributed energy resources within clearly defined electrical boundaries, which act as a single controllable entity with respect to the grid. A microgrid can connect and disconnect from the grid to enable it to operate in both grid-connected and islanded-modes” [17]. Overview of a possible microgrid solution is shown in figure 1.8.

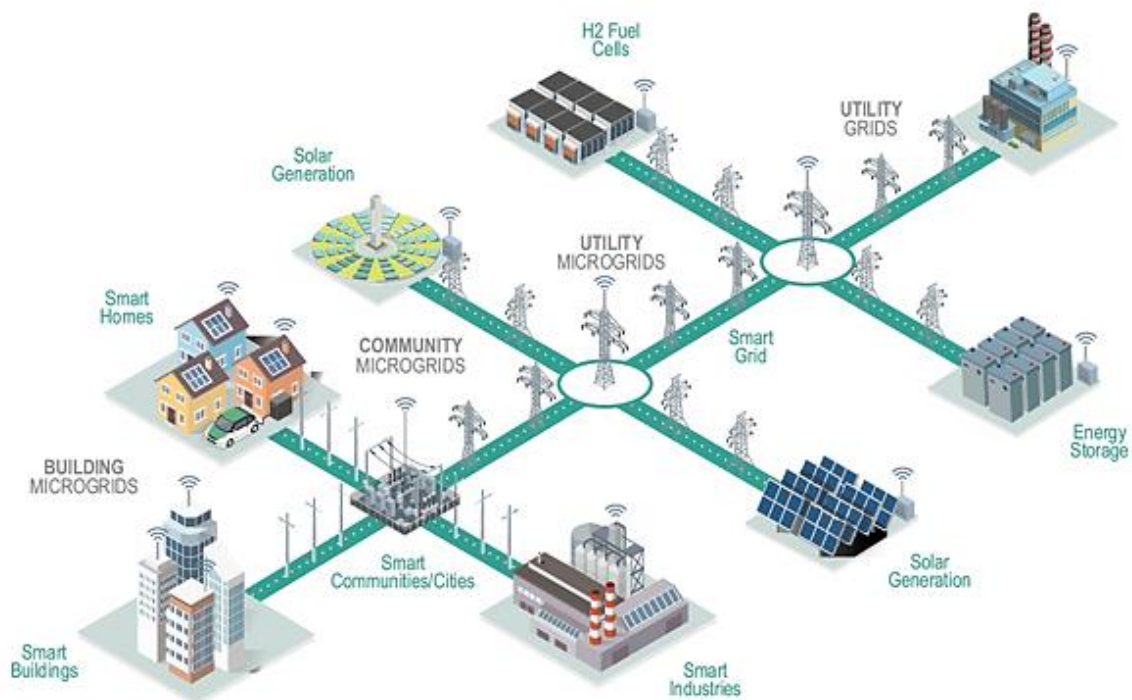


Figure 1.8 Overview of a possible microgrid solution [18]

As stated by the definition, microgrids can be composed of many different loads and distributed energy resources (DER) such as photovoltaic (PV) panels, wind plants, diesel generators, battery banks, flywheel systems, etc.

Nearly zero energy buildings (nZEB) can be considered as a part of a microgrid. As to accomplish nearly zero energy balance means that most nZEB utilize some form of on-site generation and storage that could be integrated in a microgrid as DER.

The European Union (EU) has set out directive that requires by the end of 2020 that all new buildings should be nZEB [3]. The same directive used a definition for nZEB as “a building that has a very high energy performance. The nearly zero or very low amount of energy required should be covered to a very significant extent by energy from renewable sources, including energy from renewable sources produced on-site or nearby” [3].

From the nature of the distributed generation (DG) taking place in microgrids and grid-connected nZEB, it follows that the production and consumption must be coordinated effectively. Renewable energy sources, such as solar and wind, are fluctuating and unpredictable, just as the consumption is too. Balancing generation and load becomes an important issue, as the unbalance results in deviations of grid parameters such as voltage and frequency. Especially in microgrids as they tend to have small inertia due to their smaller size compared to conventional large grids. The grid unbalance can be further aggravated in weaker microgrids and nZEB that have a suboptimal power infrastructure.

Long term balance differences that occur during the noon when renewable energy production is highest and consumption low can be mitigated to some extent with demand side management (DSM). DSM is a process when the loads of the consumers are shifted around from one time of the day to another based on some control method such as price-based control. If poorly implemented the DSM can however result in a simultaneous turn on of loads that can further disrupt the grid balance.

All these balancing problems discussed above mean that a more active solution is needed. To effectively balance production and consumption an energy storage is preferably installed. That storage should be based on a technology that can supply or draw power quickly as to react to fast changes in the grid parameters. Flywheel energy storage was chosen in this work due to its relatively high power and durability to withstand many charge cycles as compared to other competing storage technologies discussed in chapter 1.2.

## 2. DEVELOPMENT OF FESS MODEL

### 2.1 Modeled physical components

The components used in this work can be divided into two separate categories: the components of the flywheel system and the components of the grid

The flywheel model consists of an asynchronous machine, bidirectional AC/DC converters and filtering blocks. The grid model is made of a three-phase programmable voltage source, a transformer and a variable load. The Matlab code used to model the flywheel system is shown in appendix 1 and the Simulink model of physical components is shown in appendix 2.

#### 2.1.1 Flywheel system

The **motor-generator** unit was modeled using a pre-made *Asynchronous machine* block. The parameters used for the motor model had to be as close as possible to the real induction machine. However, values for some parameters such as stator and rotor resistances and inductances were not given in the flywheel system datasheet. Values were needed for a 2 pole 15 kW squirrel-cage motor that operates at 400 V phase-to-phase voltage, 50 Hz frequency with a nominal rotational speed of 3000 rpm. For this a default preset (preset 17) from *Asynchronous machine* block was used as a base and modified to match the desired parameters. Stator inertia was modified to include the flywheel inertia and the pole numbers were changed from 4 to 2. Parameters used for the *Asynchronous Machine* block are shown in table 2.1 with modified values in bold and default values in parenthesis.

Table 2.1 Parameters used for the *Asynchronous Machine* block

Parameter	Symbol	Value
Nominal power	$P_n$	15 kVA
Voltage (phase-to-phase)	$U_{LL}$	400 V
Nominal frequency	$f_n$	50 Hz
Stator resistance	$R_s$	0,2147 $\Omega$
Rotor resistance	$R_r$	0,2205 $\Omega$
Stator leakage inductance	$L_{ls}$	0,000991 H
Rotor leakage inductance	$L_{lr}$	0,000991 H
Mutual inductance	$L_m$	0,06419 H
Stator inertia	$J$	<b>2,162</b> (0,102) kgm <sup>2</sup>
Friction factor	$F$	<b>0,004</b> (0,009541) Nms
Pole pairs	$p$	<b>1</b> (2)

**Bidirectional AC/DC converters** were modeled using a *Universal Bridge* block that offers a wide selection of different power electronic devices such as: diodes, thyristors, GTOs, MOSFETs, IGBTs, etc. For this work a combination of IGBTs and diodes was used to allow bidirectional power flow. Diodes act as rectifiers during the AC/DC operation and IGBTs as inverters during DC/AC operation. As a single converter can only convert between AC and DC then to perform the necessary AC/AC conversion it is needed to connect two bidirectional AC/DC converters back to back with a dc-link in between to smooth out voltage fluctuations. One converter works as a rectifier and other as an inverter depending on the flywheel charging or discharging operation as discussed previously in chapter 1.1.5. The space vector modulated switching control of IGBTs for the inverting process is discussed in the following in chapter 2.2.5. Parameters used for the *Universal Bridge* block are shown in table 2.2 with modified values in bold and default values in parenthesis.

Table 2.2 Parameters used for the Universal Bridge block

Parameter	Symbol	Value
Snubber resistance	$R_s$	$10^5 \Omega$
Snubber capacitance	$C_s$	Inf
On resistance	$R_{on}$	$10^{-3} \Omega$
Forward voltages	device $V_f$ , diode $V_f$	<b>0,7 0,7</b> (0 0) V

**Dc-link capacitor** is located in the intermediate dc bus between the two AC systems. It is needed to smooth out the harmonics and distortions to provide a good quality DC source for the inverter. It also acts as a small energy storage between the flywheel and the grid providing increased flexibility to the independently controlled energy flow of motor-side and grid-side converters by allowing the dc voltage to be kept within allowed limits for longer time.

The dc-link capacitance can be calculated using equation 2.1 [19].

$$C = \frac{P_{motor}}{12 * f_{AC} * \Delta_U * U_{DC}} \quad (2.1)$$

where  $P_{motor}$  – nominal power of the motor drive, W,

$f_{AC}$  – frequency of the AC source, Hz,

$\Delta_U$  – desired voltage ripple, V,

$U_{DC}$  – average desired dc-link voltage, V.

For this work a dc-link capacitor with a capacitance of 3500  $\mu\text{F}$  was used, rounded from 3571  $\mu\text{F}$  that was calculated using equation 2.1 by setting the nominal power of the motor drive as 15 kW, frequency of the AC source as 50 Hz, desired voltage ripple as 10 V and average desired dc-link voltage as 700 V.

**LCL filters** are one of the more commonly used filters for grid-interconnected systems. They are located between the grid and the grid-side converter to smooth out the pulse width modulated voltage output and the current draw impulses. LCL filters are commonly considered as a better choice than L or LC filters due to their higher attenuation after the cutoff frequency and their overall lower weight and size [20].

The values for the components of the LCL filter were calculated based on the system parameters of the flywheel system used in this work: inverter power rating  $P_n = 15$  kW, grid phase-to-phase voltage  $U_{LL} = 400$  V, dc-link voltage  $U_{DC} = 700$  V, grid frequency  $f_{AC} = 50$  Hz and converter switching frequency  $f_{sw} = 16$  kHz.

Equations 2.2 to 2.11 were used to design the filter [20]. First the system parameters were converted into base values, the base impedance  $Z_b$  and the base capacitance  $C_b$  were calculated using equations 2.2 and 2.3 respectively.

$$Z_b = \frac{U_{LL}^2}{P_n} \quad (2.2)$$

$$C_b = \frac{1}{2\pi f_{AC} Z_b} \quad (2.3)$$

The filter capacitance  $C_f$  was calculated with equation 2.4 to be 2,984  $\mu$ F and rounded to 3  $\mu$ F. The variable  $x$  denotes the maximum power factor variation seen by the grid, which was set to 0,01 (1%) to compensate the inductive reactance of the filter. The equation 2.4 calculates filter capacitances for the star configuration used in this work, for the delta configuration the capacitances would have to be divided by 3.

$$C_f = x C_b \quad (2.4)$$

The inductance  $L_i$  of the inverter-side inductor was calculated using equation 2.5 to be 6,187 mH and rounded to 6,2 mH. The variable  $\Delta I_{Lmax}$  stands for the maximum peak-to-peak current ripple of the inverter output that was calculated using equation 2.6 to be 0,02 (2%) of the maximum rated current  $I_{max}$ .

$$L_i = \frac{U_{DC}}{6f_{sw}\Delta I_{Lmax}} \quad (2.5)$$

$$\Delta I_{Lmax} = 0,02 I_{max} = 0,02 \left( \frac{P_n \sqrt{2}}{3U_{LL}} \right) \quad (2.6)$$

The inductance  $L_g$  of the grid-side inductor was calculated using equation 2.7 to be 0,1989 mH and rounded to 0,2 mH where the variable  $k_a$  stands for the attenuation rate of the filter, which was set as 0,2 indicating a 20 dB drop per decade in amplitude of the current after the cutoff frequency.

$$L_g = \frac{\sqrt{\frac{1}{k_a^2} + 1}}{2\pi f_{sw}^2 C_f} \quad (2.7)$$

In order for the filter to provide good enough filtering its cutoff frequency  $f_0$  has to be well below the switching frequency  $f_{sw} = 16$  kHz, however due to resonance problems it also has to be well above the grid frequency  $f_{AC} = 50$  Hz. The cutoff frequency for the designed LCL filter was calculated using equation 2.9 to be 6584 Hz which is in compliance with the engineering *best practice* set by condition 2.10 [20].

$$f_0 = \frac{1}{2\pi} \sqrt{\frac{L_i + L_g}{L_i L_g C_f}} \quad (2.9)$$

$$10f_{AC} < f_0 < 0,5f_{sw} \quad (2.10)$$

However, because the impedance of the LCL filter is zero at the resonance frequency it can cause undesired problems such as oscillations. Often a dampening resistor is employed to insert impedance at the resonance frequencies. The resistors were set in series with the capacitors and their resistance  $R_d$  was calculated to be 2,7  $\Omega$ , one third of the impedance of the filter capacitors at the resonant frequency as shown in equation 2.11. This equation calculates values for dampening resistors used in a star configuration; as it is in this work, for the delta configuration the resistances would have to be multiplied by 3.

$$R_d = \frac{1}{3} \cdot \frac{1}{2\pi f_0 C_f} \quad (2.11)$$

The system and LCL filter parameters used for the models in this work are compiled into tables 2.3.and 2.4 respectively.

Table 2.3 System parameters

System Parameters	Symbol	Value
Grid phase-to-phase voltage	$U_{LL}$	400 V
Grid frequency	$f_{AC}$	50 Hz
DC-link voltage	$U_{DC}$	700 V
Inverter switching frequency	$f_{sw}$	16 kHz
Inverter power rating	$P_n$	15 kW

Table 2.4 LCL filter parameters

LCL Filter Parameters	Symbol	Value
Inverter-side inductor	$L_i$	6,2 mH
Grid-side inductor	$L_g$	0,2 mH
Filtering capacitor	$C_f$	3 $\mu$ F
Dampening resistor	$R_d$	2,7 $\Omega$

The performance of the LCL filter was evaluated by measuring the total harmonic distortion (THD) of the converter output voltage and current. THD was measured at multiple different active and reactive power flow configurations. The worst case scenario was seen when the converter was supplying purely active power. The harmonic contents of the supplied voltage changed very little with different power levels 0,62% at 5 kW and 0,65% at 15 kW. However, the harmonic contents of the current were much higher at low power levels, 3,48% at 5 kW and 1,00% at 15 kW.

### 2.1.2 Grid model description

The **electrical grid** outside of the simulated microgrid was modeled using a *Three-Phase Programmable Voltage Source* block. That voltage source block is programmable in a sense that parameters such as amplitude, phase and frequency are adjustable during the simulation time. The adjustability of the outside grid was necessary to simulate the use of a flywheel system for power conditioning during undesirable grid conditions or interruptions as stated by the objective of this work. The outside electrical grid was modeled to operate at a phase-to-phase voltage of 6 kV and a frequency of 50 Hz.

The **step down transformer** was modeled using a *Three-Phase Transformer (Two Windings)* block. The purpose of it was to step down the 6 kV transmission system voltage to a distribution system voltage of 400 V. Some of the transformer parameters were changed for this work. Transformer nominal frequency was changed to 50 Hz and winding voltages for primary and secondary were set 6 kV and 400 V respectively. Depending on the simulation scenario described later in chapter 3 the transformers nominal power parameter was adjusted to simulate either a strong grid or a weak grid, whenever needed.

**Consumers** / load had to be modeled for use in the simulation scenarios. A variable load was needed to model a realistic dynamic system where consumption varies and as a result also grid parameters such as voltage vary. Simulink only offers pre-made blocks for constant loads that cannot change during the simulation. Therefore, a variable load block had to be modeled entirely.

Creation of a variable load model was approached by using *Controlled Current Source* blocks. Current must be drawn from the grid in order to simulate a load. This was achieved by generating a current sine wave in opposite phase with the voltage. The amplitude of the current sine determined the active power draw while the phase difference in current and voltage sines determined the reactive power draw. For this work, only active power loads were considered.

To construct a current sine in opposite phase with voltage, first it was needed to know the phase angle of the grid voltage; this was obtained by using a Phase Locked Loop (PLL). Based on the reference values for the active power load  $P_{load}$  the amplitude of the current sine wave  $i_{load}$  was calculated by using the equation 2.12

$$i_{load} = \frac{P_{load}\sqrt{2}}{230 * 3} \quad (2.12)$$

By knowing the phase angle of the grid voltage and the amplitude of the current needed for the desired load the reference sine waves for the *Controlled Current Source* block were constructed. The Simulink model for the variable load block is shown in appendix 3.

The load profiles used later in simulation scenarios for the consumers originate from one second power measurements in the NRG building of Tallinn University of Technology.

## 2.2 Converter control strategies

The active and reactive power draw commands are the only variables of the flywheel energy storage system that are supposed to be controllable from the outside either by human or some control system. In this work, the power draw commands came from the algorithms of the simulation scenarios discussed later in chapter 3. To accomplish controllable power flow between the flywheel and the grid, both of the converters used in the flywheel system had to be operated together; however, since they have their own different roles, the control algorithms used for them were different.

The objective of controlling the grid-side converter is to output the commanded power, this is done by regulating the power flow between the grid and the dc link capacitor. This however results in either increase or decrease of the dc-link voltage and from that follows that the purpose of controlling the motor-side converter is to regulate the dc-link voltage by either consuming or releasing energy by accelerating or decelerating the flywheel.

The joint control of the converters is described in the FESS Control Unit chapter 2.2.1. The speed and field oriented control of the MSC are discussed in chapters 2.2.2 and 2.2.4 respectively. The current control of the GSC is discussed in chapter 2.2.6.

### 2.2.1 FESS control unit

The purpose of FESS Control Unit (FCU) is to control both of the converters together during different flywheel operation states. The MSC is controlled by the FCU through rotor speed reference  $\omega_{ref}$  values supplied to the speed controller, which determines the torque and rotor flux references  $T_{ref}$  and  $\psi_{r\_ref}$  respectively. The GSC is controlled by active  $P_{ref}$  and reactive  $Q_{ref}$  power reference values forwarded to the current controller. The block scheme describing the converter control strategy is shown in figure 2.1 and Simulink implementation is shown in appendix 4.

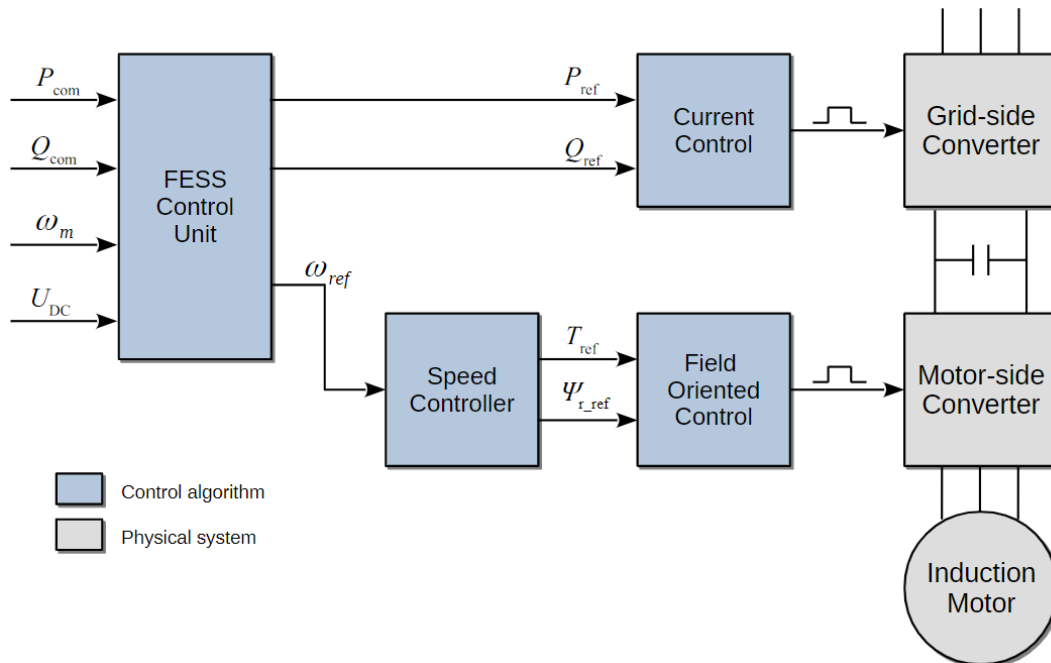


Figure 2.1 Block diagram of converter control strategy

**The state selection logic** is what determines the operational state that the flywheel system is supposed to be in based on the power draw command and the rotational speed of the flywheel. The flywheel system modeled in this work has three different operating states: the startup state, the standby state and the motoring/regen state.

The simplified algorithm used for the state selection logic is depicted in figure 2.2, its conditions are checked every timestep of the simulation. The Simulink implementation of this algorithm is shown in appendix 5.

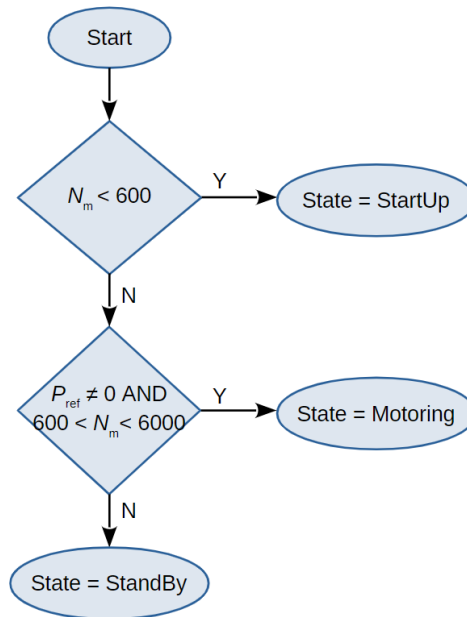


Figure 2.2 The algorithm for the state selection of the flywheel system

The startup state is determined by the rotational speed  $\omega_m$  of the flywheel. If it is below 600 rpm then the startup state is turned on and the flywheel accelerates until it reaches the minimum operational speed of 600 rpm.

The logic for the motoring/regen state checks if the flywheel is within the minimum and maximum operational speed range of 600 rpm and 6000 rpm respectively and whether power is being requested to be absorbed ( $P_{ref} < 0$ ) or released ( $P_{ref} > 0$ ) by the flywheel system. The speed check also limits the flywheel from over- or under-speeding during its motoring/regen operation.

If the conditions set by the startup or motoring/regen state are not met, it means that the flywheel system is within its operational speed range, but there is no power draw request, meaning that it should go to the standby state and await until power is being requested.

**The control of the operating modes** themselves was modeled while considering an induction machine's (IM) operating characteristics shown in figure 2.3. When operating below the nominal speed of the IM, the nominal power draw or supply cannot be achieved, instead it is linearly proportional to the speed of the rotor.

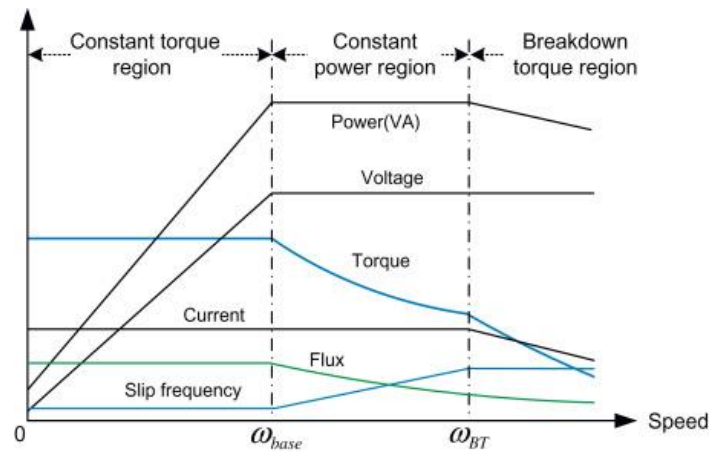


Figure 2.3 Operating characteristics of an induction machine [21]

The objective of the startup mode is to accelerate the flywheel up to its minimum operational speed. This acceleration is done using constant torque as operations below nominal speed take place in constant torque region. While the MSC draws energy for the motor the GSC is set to regulate the dc-link voltage. In a startup mode the rotor speed is the important variable to be controlled while the power draw in itself is of a lesser importance. The startup mode was implemented in the Simulink through the FCU, setting the reference speed to be reached as 600 rpm and forwarding it to the *Speed controller* that limits its outputted torque to a constant value for a constant torque acceleration. At the same time the power flow reference values for the GSC were determined by the FCU by using a proportional-integral (PI) controller to regulate the dc-link voltage back to 700 V. The gains of the PI were manually tuned to  $k_p = 500$  and  $k_i = 5000$ . The Simulink model for startup mode is shown in appendix 6.

During the motoring/regen mode the important variables to be controlled are reversed. As during its normal operation the flywheel system is commanded to either supply or draw specific amount of power, then the power flow of the GSC becomes an important variable while the rotor speed holds lesser of an importance, as long as it stays within the normal operational region. However, the flywheel speed of course determines the duration that the flywheel system is able to draw or supply its power. The Simulink model of the motoring/regen mode consisted of one PI controller again to control the dc-link voltage, which is maintained by regulating the flywheel speed. The gains for this PI were manually tuned to  $k_p = 0,5$  and  $k_i = 10$ . The power flow commands received by the FCU were forwarded to the current control of the GSC. However, as discussed previously, the induction motor based flywheel system has reduced power available below the nominal operational speed. The power flow commands were then limited to the maximum amount possible at that rotor speed with equation 2.13. The nominal speed of the IM used in this work is 3000 rpm

and the nominal power 15 kW. The Simulink model for motoring and regen mode is shown in appendix 7.

$$P_{\max} = \frac{N}{N_{\text{nom}}} P_{\text{nom}} \quad (2.13)$$

Where  $N$  – measured rotor speed, rpm,

$N_{\text{nom}}$  – nominal rotor speed, rpm,

$P_{\text{nom}}$  – nominal power, kW.

If the flywheel system is in neither the startup nor motoring/regen mode, then the standby mode is activated. During the standby the dc-link voltage becomes the important variable to regulate. In this work, the flywheel system was designed to maintain its rotational speed when entering the standby mode. However, to maintain its speed some power must always be supplied to the flywheel system, because of the air friction losses, winding heat losses and the power needed to maintain the magnetic fields. There are also other designs where the flywheel system is let to *run down* during the standby mode. This would be more suitable for a long-term storage application using efficient high-speed vacuum enclosed flywheel systems, rather than the power conditioning applications using low-speed flywheel discussed in this work.

The standby mode was modeled in Simulink with a PI controller that tries to maintain the dc-link voltage by instructing the GSC to draw the necessary power to cover the running losses. The gains for this PI were manually tuned to  $k_p = 0,5$  and  $k_i = 10$ . The Simulink model for standby mode is shown in appendix 8.

In order to evaluate the performance of the modeled flywheel system a verification test was simulated. Figure 2.4 shows the measured rotor speed, grid power draw and dc-link voltage of the simulation.

At the beginning of the simulation the FCU correctly set the flywheel system into a startup mode and the flywheel accelerated to 600 rpm within 3,3 seconds, after which it entered the standby mode. At the simulation time of 4 seconds the flywheel system was then instructed to be charged at full power for 6 more seconds and at the simulation time of 11 seconds to be discharged at full power until the minimum operation speed was reached.

From the grid power draw graph, it can be seen that even though the flywheel system was instructed to charge and discharge at full power, the power flow was proportional to the rotational

speed of the flywheel, as mentioned previously, the system has reduced power available below the nominal speed of 3000 rpm.

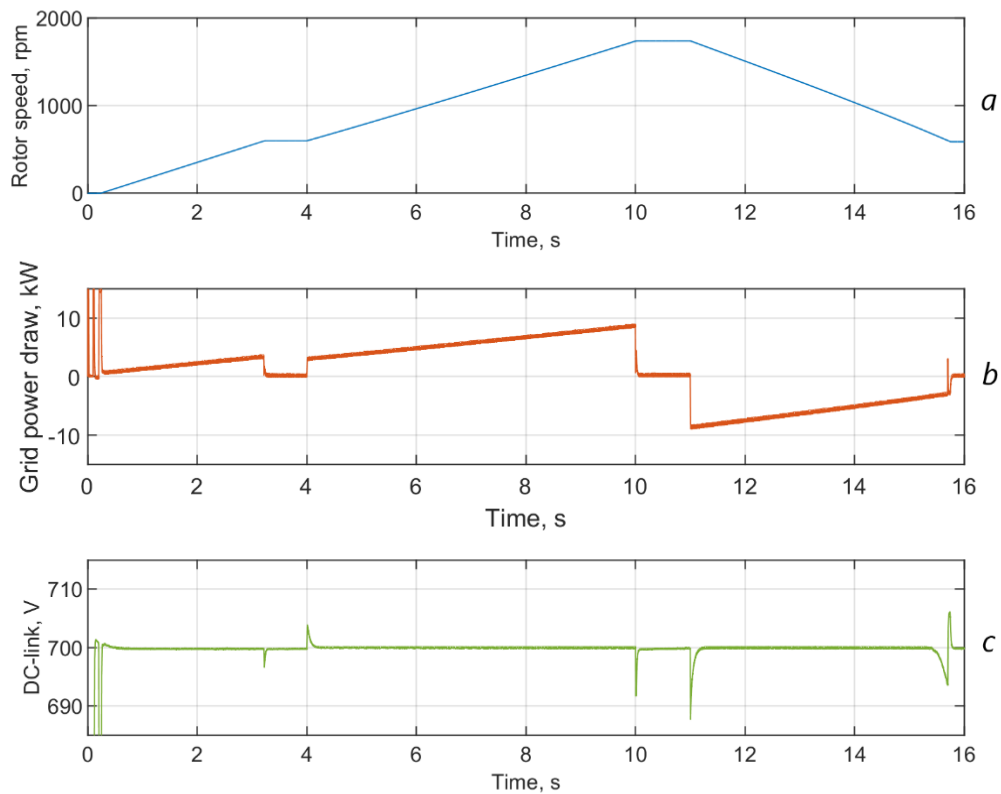


Figure 2.4 Test run of the flywheel system: a) flywheel rotor speed, b) grid power draw, c) dc-link voltage

The dc-link voltage graph shows that the voltage regulation performance of the system is adequate, with spikes of 10 V appearing during the state changes of the flywheel system. The dc-link voltage remained well between the minimum of 566 V and maximum of 780 V. The allowed range of the dc-link voltage is discussed further in chapter 2.2.5.

According to the datasheet the round-trip efficiency of Rosetta T3-15 flywheel system is 77,6%. From the test run the round-trip efficiency of the system was calculated to be 80,2% by comparing the energy drawn from the grid during the acceleration to the energy supplied to the grid while discharging. Energy drawn and supplied was evaluated by integrating the power draw from the start to the stop of the motoring and regen states, as energy is power over time and can also be thought as the area under the power curve.

## 2.2.2 Speed controller

Control of the MSC consists of the *Speed controller* blocks and the *Field Oriented Control* blocks connected back-to-back.

The goal of the speed control block is to output the reference values of torque and flux for the field oriented control. The torque reference value was determined by the error between the rotor speed reference  $N_{ref}$  and the measured rotor speed  $N$ . This speed error  $N_{err}$  was then fed into a PI controller that tried to minimize the speed error by outputting a corresponding torque reference  $T_{ref}$ . The gains used for the speed control PI  $k_p = 20$  and  $k_i = 0,09$  were obtained through manual tuning. The torque reference signal was then passed through a low-pass filter to prevent rotor oscillations and finally limited to a maximum of 60 Nm and minimum of -60 Nm to prevent overloading as according to the datasheet of Rosetta T3-15 flywheel system.

Speed control was modeled by modifying a pre-existing Simulink *Speed Controller (AC)* block. The modifications were done to simplify its operation as it contained functions not needed for the purpose of this thesis. The working principle of the used speed controller is shown in figure 2.5 and the Simulink implementation is shown in appendix 9.

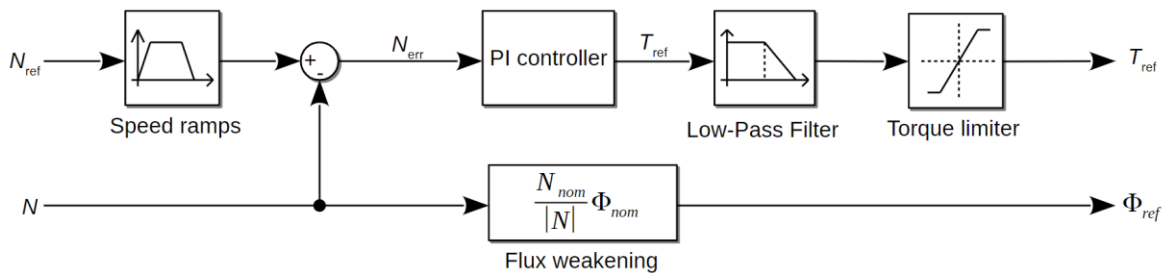


Figure 2.5 Working principle of the speed controller

The 2-pole induction motor used in this work has a nominal speed of 3000 rpm. However, the flywheel system is rated to operate at up to 6000 rpm which means that the induction motor must be able to operate above nominal speed. The magnetic field flux must be weakened at operations above nominal speed to counteract the increasing back-emf [22]. The field weakening was achieved by regulating the flux reference  $\Psi_{ref}$  using equation 2.14.

$$\Psi_{ref} = \frac{N_{nom}}{|N|} \Psi_{nom} \quad (2.14)$$

where  $\Psi_{nom}$  – nominal flux, Wb,

$N_{nom}$  – nominal speed, rpm.

The Rosetta T3-15 flywheel datasheet did not describe the nominal flux for the motor. According to the literature the nominal flux of an asynchronous machine should be proportional to the ratio of nominal voltage and frequency as shown in equation 2.15 [23].

$$\psi_{\text{nom}} = \frac{U_{\text{nom}}}{2\pi f_{\text{AC}}} \quad (2.15)$$

By substituting  $U_{\text{nom}} = 400 \text{ V}$  and  $f_{\text{AC}} = 50 \text{ Hz}$  into equation 2.15 the nominal flux was calculated to be 1,27 Wb. However, the torque produced by the motor at above nominal speed was oscillating and unstable. Multiple test simulations were conducted around the calculated nominal flux and the best results were seen with the value 1,2 Wb as higher or lower values made the motor operations unstable either during the high-speed motoring or low speed regenerative braking

A test run simulation was conducted to evaluate the capabilities of modeled speed controller. The test run consisted of a simple 250 rpm/s ramp acceleration up to 125 rpm and deceleration back to standstill. Figure 2.6 shows the ramp response of the test run. The speed error is small with about 2,5 rpm during the transient period and becomes negligible within 25 ms during the steady state operation.

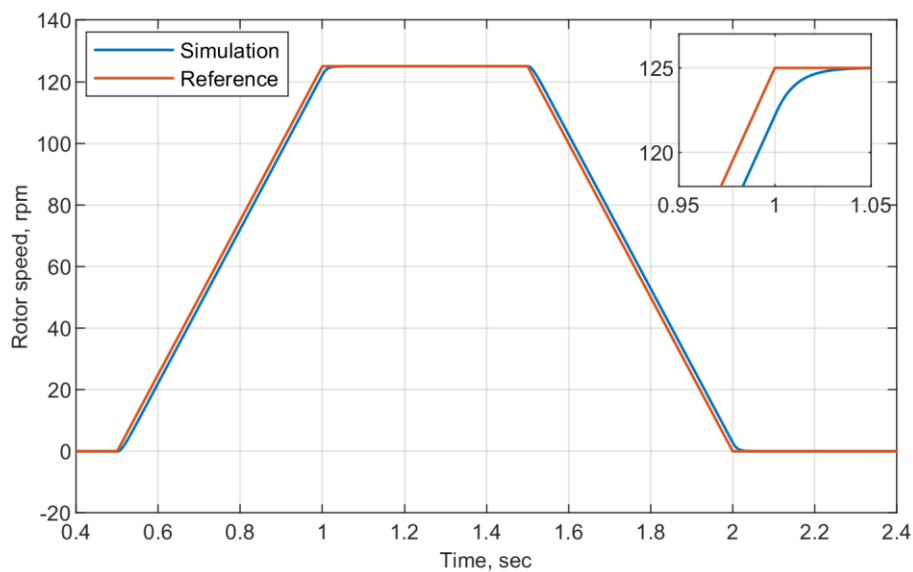


Figure 2.6 Ramp response of the flywheel speed control test run

### 2.2.3 Clarke and Park transforms

Clarke and Park transforms are commonly used to simplify three-phase sinusoidal systems. It is difficult to control constantly varying AC signals using PID or PI controllers, thus converting them into constant valued DC signals simplifies the computation and control of the those systems [24]. These transforms also decouple active and reactive components of the currents, allowing separate control of the motor flux and torque in the field oriented control of the motor-side converter [25] while also allowing separate control of the injected active and reactive power in the current control of the grid-side converter [26]. Figure 2.7 illustrates the differences of natural, stationary and rotating reference frames.

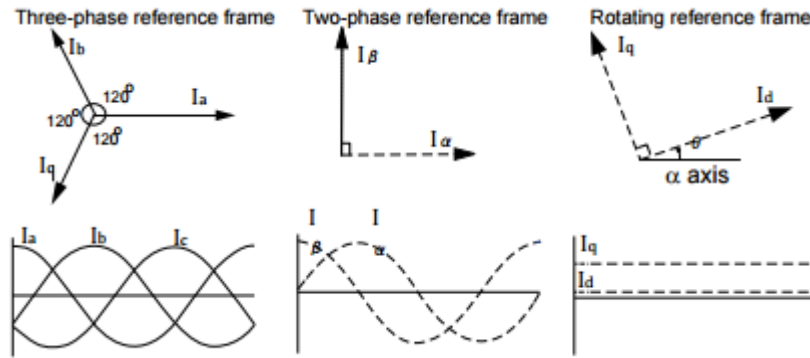


Figure 2.7 Phasor diagrams of natural ( $abc$ ), stationary ( $\alpha\beta$ ) and rotating ( $dq$ ) reference frames [27]

Using the Clarke transform it is possible to simplify the three-phase natural ( $abc$ ) reference frame by converting it into two-phase ( $\alpha\beta$ ) stationary reference frame, where the vectors  $\alpha$  and  $\beta$  are located orthogonally and vary by their magnitude. Clarke transform can be implemented using equation 2.16 [28].

$$\begin{bmatrix} \alpha \\ \beta \\ 0 \end{bmatrix} = \frac{2}{3} \begin{bmatrix} 1 & -\frac{1}{2} & -\frac{1}{2} \\ 0 & \frac{\sqrt{3}}{2} & -\frac{\sqrt{3}}{2} \\ \frac{1}{2} & \frac{1}{2} & \frac{1}{2} \end{bmatrix} \begin{bmatrix} a \\ b \\ c \end{bmatrix} \quad (2.16)$$

where  $\alpha\beta$  – components of the stationary reference frame, V,

0 – zero component of the stationary reference frame. V,

$abc$  – components of the  $abc$  reference frame, V.

This system can be further simplified by using Park transform to either convert directly from the natural ( $abc$ ) reference frame or from the two-phase ( $\alpha\beta$ ) stationary reference frame into a ( $dq$ ) rotating reference frame, where  $d$  and  $q$  vectors are in constant magnitude while rotating around the center axis. Often times the rotating reference frame is fixed to rotate synchronously with some other system such as the rotor of an electric motor to reduce the system complexity even further. Park transformation can be realized using equation 2.17 [29].

$$\begin{bmatrix} d \\ q \\ 0 \end{bmatrix} = \frac{2}{3} \begin{bmatrix} \sin(\theta) & \sin\left(\theta - \frac{2\pi}{3}\right) & \sin\left(\theta + \frac{2\pi}{3}\right) \\ \cos(\theta) & \cos\left(\theta - \frac{2\pi}{3}\right) & \cos\left(\theta + \frac{2\pi}{3}\right) \\ \frac{1}{2} & \frac{1}{2} & \frac{1}{2} \end{bmatrix} \begin{bmatrix} a \\ b \\ c \end{bmatrix} \quad (2.17)$$

where  $dq$  – components of the rotating reference frame, V,

0 – zero component of the stationary reference frame, V,

$abc$  – components of the  $abc$  reference frame, V.

## 2.2.4 Field oriented control of motor-side converter

Compared to AC machines DC machines have a relatively simple control strategy, as they naturally allow for independent control of torque and flux. Using permanent magnets the DC machine control simplifies even further as only the torque forming current needs to be controlled. Therefore, the early control algorithms of electric motors were mostly developed for DC machines due to their computational simplicity. Later however field oriented control was developed to make AC machines controllable like DC machine such as that both the torque and flux could be controlled independently by decoupling the currents that form torque and flux [25].

According to the Rosetta T3-15 datasheet a closed-loop vector control is used, meaning that rotor speed is being measured and used as a feedback for the control algorithm. However, because the magnetic fields are not being measured directly, then this type of FOC is called indirect field-oriented control (IFOC) [30].

Field-oriented control was modeled based on a pre-existing *Field-Oriented Controller* block that offers both average and detailed models with either space vector modulation (SVM) or hysteresis modulation type. For this work a detailed model with SVM was used and its Simulink model is shown in appendix 10. The schematic diagram of the indirect field-oriented control algorithm used in this work is shown in figure 2.8, it was created based on the Simulink model.

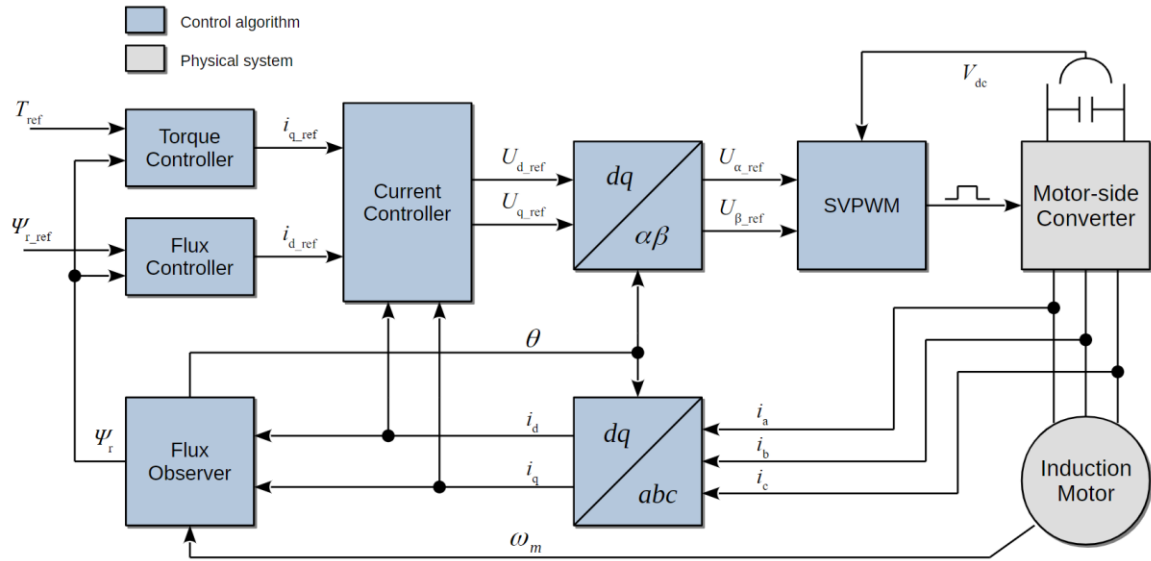


Figure 2.8 Schematic diagram of indirect field oriented control

The FOC algorithm shown above consists of following components: space vector pulse width modulation (SVPWM) block, Park and Clarke transform blocks, current, torque and flux controller blocks and flux observer block.

As stated earlier the idea of FOC is to decouple the control of torque and flux, this is achieved by regulating the torque forming current  $i_q$  and the flux forming current  $i_d$  independently. The reference values for these currents  $i_{q\_ref}$  and  $i_{d\_ref}$  are generated by the *Torque Controller* and the *Flux Controller* blocks respectively. The reference values for the torque  $T_{ref}$  and the rotor flux  $\Psi_{r\_ref}$  themselves are produced by the *Speed Controller* block described in chapter 2.2.2. The *Torque Controller* block calculates values for the current reference  $i_{q\_ref}$  using equation 2.18 [31].

$$i_{q\_ref} = \frac{2}{3} \frac{1}{n_p} \frac{L_r}{L_m} \frac{T_{ref}}{\Psi_r} \quad (2.18)$$

where,  $n_p$  – number of motor poles pairs;

$L_r$  – rotor inductance, H,

$L_m$  – mutual inductance, H,

$\Psi_r$  – rotor flux, W<sub>b</sub>,

$T_{ref}$  – torque reference, N<sub>m</sub>.

The *Flux Controller* block evaluates the current reference  $i_{d\_ref}$  by comparing rotor flux reference  $\Psi_{r\_ref}$  from the *Speed Controller* block to the rotor flux  $\Psi_r$  from the *Flux Observer* block. Due to it being an indirect field oriented control model as the rotor flux is not measured directly it has to be

approximated using other variables. Rotor flux  $\Psi_r$  can be calculated by solving a first order differential equation shown in equation 2.19 [31].

$$\frac{d}{dt}\Psi_r = -\left(\frac{R_r}{L_r}\right)\Psi_r + \left(\frac{L_m R_r}{L_r}\right)i_{ds} \quad (2.19)$$

The rotor flux  $\Psi_r$  can be evaluated from equation 2.19 by using a transfer function as shown in equation 2.20.

$$H(s) = \frac{\frac{L_m R_r}{L_r}}{s + \frac{R_r}{L_r}} \quad (2.20)$$

The flux error  $\Psi_{r\_err}$  between rotor reference flux  $\Psi_{r\_ref}$  and calculated rotor flux  $\Psi_r$  is then fed into a PI controller that tries to minimize the error by outputting a corresponding current reference  $i_{d\_ref}$ . The gains for the flux PI controller were manually tuned to  $k_p = 40$  and  $k_i = 30$ .

The second purpose of the *Flux Observer* is to calculate the angle of the rotating magnetic field because the motor used in this work is an asynchronous machine, meaning that the magnetic field and the rotor are not rotating synchronously. The angle of the rotating magnetic field is needed for the Park and Clarke transforms to convert stator currents to the  $dq$  reference frame and back.

In order to evaluate the magnetic field angle  $\theta$  it is first necessary to calculate the rotational speed of the magnetic field  $\omega_e$  which can be derived from the slip speed equation 2.21 [31].

$$\omega_{sl} = \omega_e - \omega_r = \left(\frac{L_m R_r}{\Psi_r L_r}\right)i_{qs} \quad (2.21)$$

It follows as such that:

$$\omega_e = \omega_{sl} + \omega_r = \left(\frac{L_m R_r}{\Psi_r L_r}\right)i_{qs} + \omega_r \quad (2.22)$$

The magnetic field angle  $\theta$  can now be obtained by integrating the rotational speed of the magnetic field  $\omega_e$  as shown in equation 2.23.

$$\theta = \int \omega_e d\omega \quad (2.23)$$

The *Current Controller* block consists of two PI controllers that compare the reference values of stator currents  $i_{q\_ref}$  and  $i_{d\_ref}$  from the commanded torque and flux to measured stator currents  $i_d$  and  $i_q$ . The error is outputted as reference for stator voltage components  $U_{q\_ref}$  and  $U_{d\_ref}$  necessary to drive the current. The PI gains for *Current Controller* were manually tuned to  $k_p = 50$  and  $k_i = 1000$  for both controllers.

The stator voltage components  $U_{q\_ref}$  and  $U_{d\_ref}$  are then transformed into  $U_{\alpha\_ref}$  and  $U_{\beta\_ref}$  components using the inverse park transform and finally forwarded to the space vector pulse width modulator (*SVPWM*) block that calculates the switching times for motor-side converter based on the voltage reference values and measured dc-link voltage as discussed in chapter 2.2.5.

The switching frequency used for field oriented control was 16 kHz as according to the datasheet of the Rosetta T3-15 flywheel system.

## 2.2.5 Space Vector Modulation

Space vector modulation (SVM) is a commonly used method of generating pulse width modulated (PWM) reference signals for inverters. The PWM gating pulses are synthesized in a way that the inverter output voltage emulates an average of the desired voltage waveform. Compared to simpler modulation techniques such as sinusoidal pulse width modulation (SPWM), the SVM provides less harmonic distortion at the output and 15,4% higher utilization of dc-link voltage [32].

At the heart of SVM is a rotating reference space vector, created as the vector sum of all the phases of the desired output voltages. Figure 2.9 (b) shows the reference space vector  $U_{ref}$  on an  $\alpha\beta$  plane of Clarke transformed desired output voltages. For a three-phase two level voltage source inverter the number of total possible switching configurations is eight as shown in figure 2.9 (a). Six of those configurations (*basic vectors*  $\vec{s}_1, \vec{s}_2, \vec{s}_3, \vec{s}_4, \vec{s}_5, \vec{s}_6$ ) represent different voltages and current directions, while two of the configurations (*zero vectors*  $\vec{s}_0, \vec{s}_7$ ) represent zero volts on the output terminals.

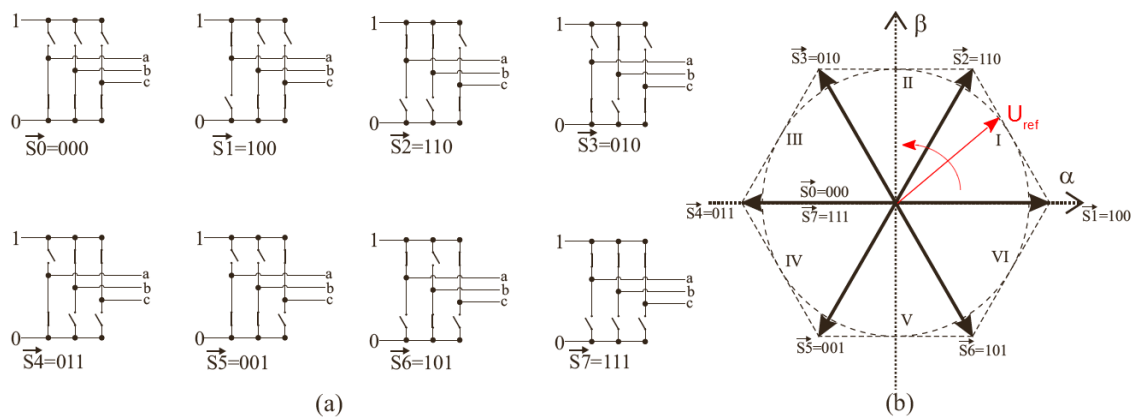


Figure 2.9 (a) Eight switching configurations, (b) Space vector diagram [33]

The phase-to-phase voltage of the inverter output can be calculated using equation 2.24.

$$U_{LL} = \frac{m_a U_{dc} \sqrt{3}}{2\sqrt{2}} \quad (2.24)$$

where  $U_{LL}$  – line-to-line (phase-to-phase) RMS voltage, V,

$m_a$  – modulation index,

$U_{dc}$  – dc-link voltage, V.

The minimum dc-link voltage needed is 566 V, it can be calculated by evaluating  $U_{dc}$  from the equation 2.24 by substituting 400 in as phase-to-phase voltage  $U_{LL}$  and 1,154 for the modulation index  $m_a$ . If the dc-link voltage should fall below that threshold the modulation index would have to rise above 1,154 resulting in the output sine wave becoming distorted and resembling more of a triangle wave [34]. According to the datasheet of Rosetta T3-15 flywheel system, the maximum allowed dc-link voltage is 780, if were to rise above that, the braking resistor would be turned on as a safety measure and the excess current would get dissipated as heat [35].

The space vector modulation was modeled in Simulink by modifying the pre-existing *Space Vector Modulator* block that was originally designed for voltage/frequency (V/Hz) control. Initially the three-phase sine references  $U_a$ ,  $U_b$  and  $U_c$  were generated by the *Three-phase generator* block that used frequency, voltage and the direction of motor rotation as inputs and then converted them into  $\alpha\beta$  reference frame. As in this work the  $U_\alpha$  and  $U_\beta$  reference sines are generated either by the field-oriented control (FOC) or the current control, the pre-existing *Three-phase generator* and *Clarke transform* blocks were not needed and removed as shown in figure 2.10.

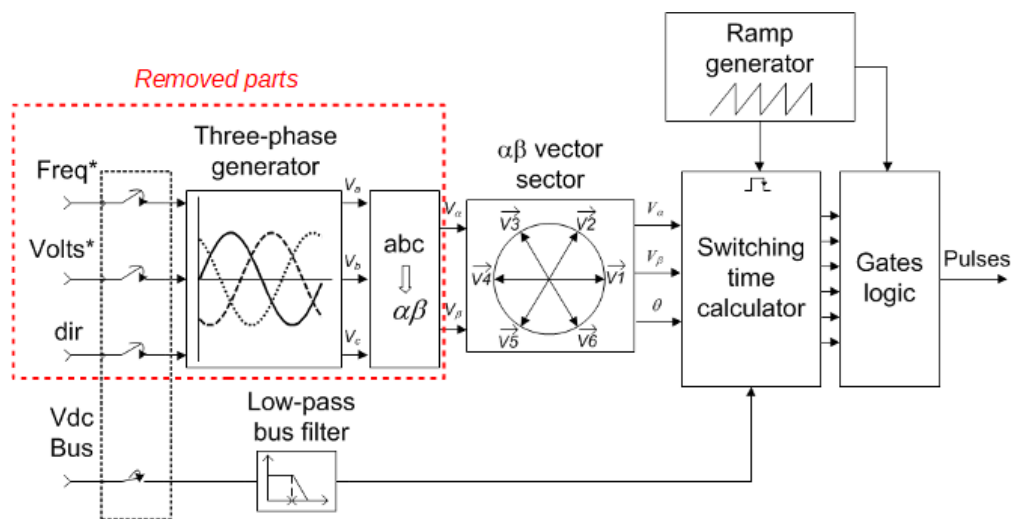


Figure 2.10 Working principle of modified *Space Vector Modulator* block used [36]

## 2.2.6 Current control of grid-side converter

The purpose of controlling the grid-side converter is to direct the power flow between the dc-link and the grid. However, when talking about the power flow it is important to differentiate between the active power and the reactive power. Independently controlling them will be useful from the view of the power conditioning as by controlling the active power flow it is possible to regulate the grid frequency and by controlling the reactive power flow it is possible to regulate the grid voltage. The active and reactive power output of the converter can be controlled independently by using the current control method [37]. Figure 2.11 shows the working principle of current control used in this work and its Simulink implementation is shown in appendix 11.

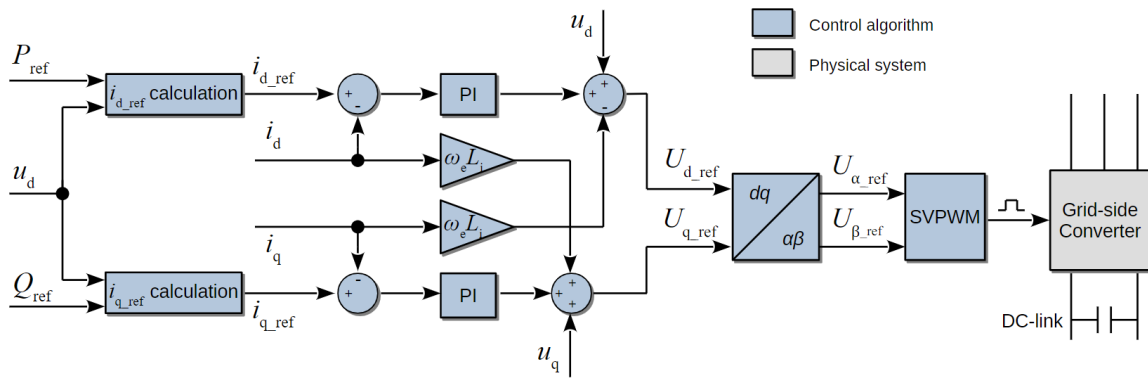


Figure 2.11 Working principle of the grid-side converter current control

The current control method is based on transforming the three-phase grid parameters  $i_{abc}$  and  $u_{abc}$  from their natural  $abc$  reference frame to the synchronously rotating  $dq$  reference frame using the Park transformation as discussed in the chapter 2.2.3. According to the instantaneous power theory the active and reactive power equations can be written in the  $dq$  reference frame using equations 2.25 and 2.26.

$$P = \frac{3}{2}(u_d i_d + u_q i_q) \quad (2.25)$$

$$Q = \frac{3}{2}(u_q i_d - u_d i_q) \quad (2.26)$$

Aligning the grid voltage with the rotating frame makes the voltage  $u_q = 0$ , the power equations then simplify to:

$$P = \frac{3}{2}u_d i_d \quad (2.27)$$

$$Q = -\frac{3}{2}u_d i_q \quad (2.28)$$

From equations 2.27 and 2.28 it can be observed that the active and reactive power can now be controlled independently by regulating the currents  $i_d$  and  $i_q$ , hence the name “current control”. In figure 2.11 the currents  $i_d$ ,  $i_q$  and the voltages  $u_d$ ,  $u_q$  are measured from the grid side of the LCL filter. The reference currents  $i_{d\_ref}$  and  $i_{q\_ref}$  are calculated based on the desired active and reactive power output of the converter received from the FESS control unit (FCU). The difference between the measured currents and reference current creates an error signal that the PI controllers try to minimize. The gains of the PI controllers were manually tuned to  $k_p = 30$  and  $k_i = 1000$ .

To understand how the output voltage references  $U_{d\_ref}$  and  $U_{q\_ref}$  are made it is necessary to first analyze the schematic of the bidirectional AC/DC converter shown in figure 2.12.

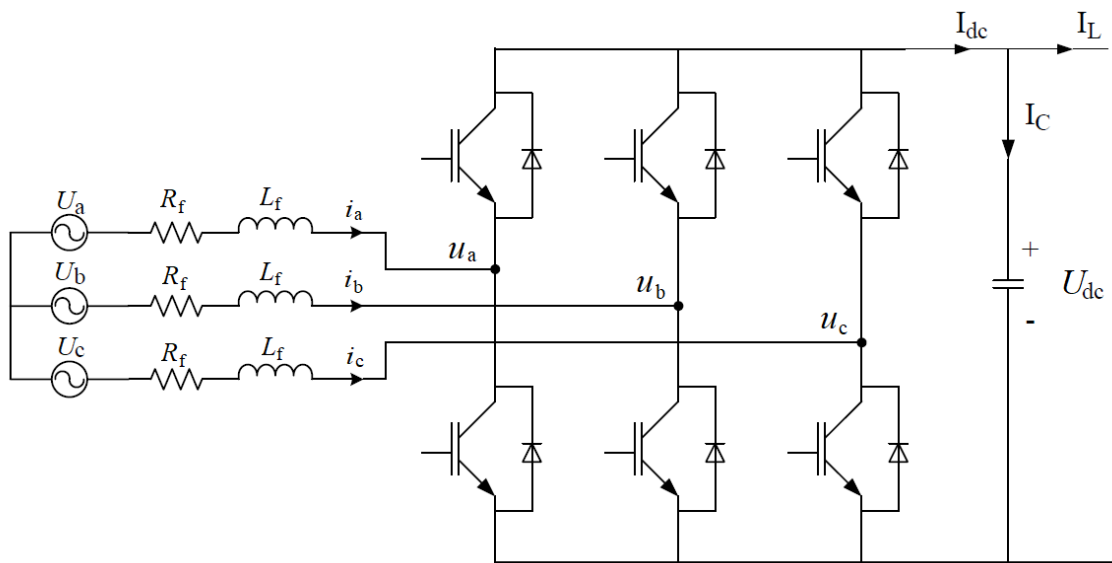


Figure 2.12 Schematic of a bidirectional AC/DC converter [38]

The voltage at the grid side of the flywheel system can be written with equation 2.29 that is derived by analyzing figure 2.12 using the Kirchhoff's voltage law.

$$U_{abc} = L \frac{d}{dt} i_{abc} + u_{abc} + R i_{abc} \quad (2.29)$$

where  $U_{abc}$  – voltage at the grid side of the filter, V,

$u_{abc}$  – converter output voltage, V,

$L$  – combined inductance of both of the filter inductors, H,

$R$  – filter resistance,  $\Omega$ .

Transforming the output voltage equation 2.29 from  $abc$  reference frame to  $dq$  reference frame using the Park transform gives us equations 2.30 and 2.31.

$$U_d = L \frac{d}{dt} i_d - \omega L i_q + u_d + R i_d \quad (2.30)$$

$$U_q = L \frac{d}{dt} i_q + \omega L i_d + u_q + R i_q \quad (2.31)$$

where  $\omega$  – grid frequency, rad/s.

Using the equations above it is now possible to control the output voltage and power of the flywheel system using the schematic shown in figure 2.11 above.

The  $dq$  frame voltage references  $U_{d\_ref}$  and  $U_{q\_ref}$  are transformed to  $\alpha\beta$  frame and forwarded to the SVPWM block that calculated the corresponding switching signals for the converter. The switching frequency used was 16 kHz, as according to the datasheet of Rosetta T3-15 flywheel system.

In order to evaluate the performance of the modeled current control of GSC a verification test was simulated. The current control is supposed to make the GSC able to output active and reactive independently. The simulation model was tested by configuring the GSC to output active and reactive power at different configurations as shown in figure 2.13.

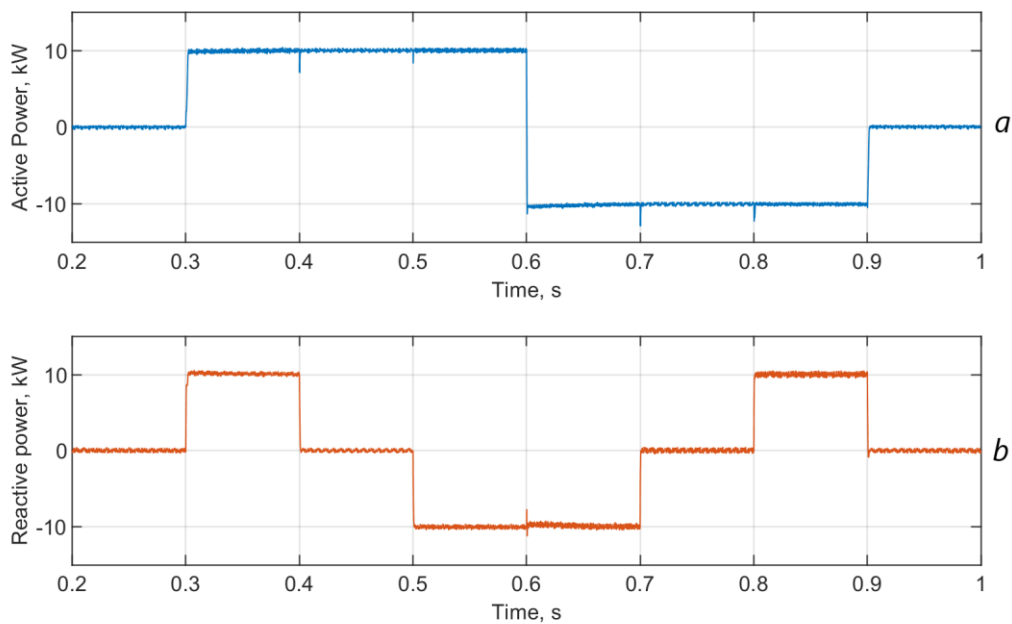


Figure 2.13 Grid-side converter power output at different configurations: a) active power, b) reactive power

The simulation proved that by using the current control the grid-side converter is indeed able to control the active and reactive power flow independently and in both directions.

The response of the converter was quick, with both 10 kW and 10 kvar transients lasting for about 1 ms. However, from the graph it can be seen that during the transient of one power type, the other power type experiences a small dip of about 3 kW or kvar.

During the steady-state operation the power oscillations were around 200 W and var. The power oscillations may be the result of fast power measurements that include the harmonic contents of voltage and current sines, 0,65% and 1,00% respectively at the rated power output as discussed previously in chapter 2.1.1.

### 3. SIMULATIONS

As stated by the title of this thesis the goal of this work is to development of power conditioning control strategies for flywheel storage in microgrid. The tested scenarios were broadly classified into two categories: off-grid and on-grid scenarios.

Figure 3.1 shows the Simulink model of the microgrid used for the simulation scenarios. It composes of a flywheel system, a consumer load, a three-phase breaker, step-down transformer and voltage source for the grid. The black bars on grid lines indicate voltage and current measurement places.

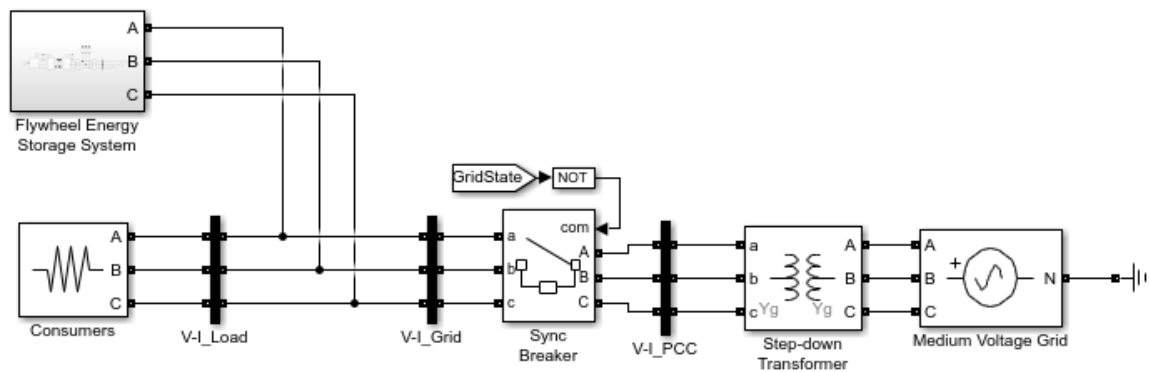


Figure 3.1 Simulink model of the microgrid used simulation scenario

#### 3.1 OFF-Grid Scenarios

Off-grid scenarios considered in this work simulate the use of a flywheel system to maintain the power during an islanded microgrid state, while also smoothing out the transition of disconnecting and reconnect with the main grid. Microgrid synchronization with the main grid was also simulated.

##### 3.1.1 Islanding / UPS

The islanding scenario simulated in this work uses the flywheel system as an uninterruptable power source to power the microgrid when there is an interruption in the supply of the main grid. The purpose of testing this scenario is to evaluate how quickly the flywheel system can take over, meaning how long will the interruption lasts. The duration that the flywheel system can sustain its power is dependent on the energy storage capacity of the flywheel used. The Rosetta T3-15 flywheel system used in this work for the base of modeling has low storage of 300 kW, meaning that the maximum power output of 15 kW can only be sustained for 20 seconds. However, this work can be used as a base to simulate higher power and more capacitive flywheel systems.

*Programmable Voltage Source* block was used to model the main grid. In order to simulate a power outage the voltage amplitude of the main grid was set to drop to zero.

The islanding was detected by measuring the main grid voltage from the point of common coupling (PCC). The measured voltage was then converted into the  $dq$  reference frame using the Park transform. Islanding detection through the natural  $abc$  reference frame was not used because measuring the root mean square (RMS) value of the voltage sine introduced a detection delay of at least 10 ms, corresponding to a half period of a sine wave. A simple islanding detection system was devised that considered grid to be failing when the  $d$  component of the grid voltage  $U_d$  dropped 10% below nominal voltage for 5 ms, a threshold of  $U_d = 292$  V that represents phase-to-neutral RMS voltage of  $U_{abc} = 207$  V. In commercial microgrids the islanding detection is far more complex, however that is beyond the scope of this work.

When an islanding was detected a three-phase circuit breaker disconnected the microgrid from the rest of the grid. This was done to operate the microgrid without the influence of the transients that might occur and be carried over from the main grid during its suboptimal operations.

During the islanded operation the power output of the grid-side converter has to be regulated automatically as the GSC has no way of knowing the power of the loads connected to the microgrid. In this work the flywheel system is the only power source during the islanded mode. Therefore, the idea of controlling GSC in this scenario is to maintain the microgrid voltage.

The required power output of the GSC needed to maintain the voltage was determined by  $dq$  components of the microgrid voltage. Reference values for them were acquired by performing a Park transform on an idealized balanced three-phase system with phase-to-phase voltage of 400V. Thus, the reference values were set as  $U_d = 325,3$  V and  $U_q = 0$  V

The voltage was regulated by two PI controllers that determined the necessary active and reactive power outputs and forwarded them to the FCU as shown in the figure 3.2. The gains of the PI controllers were manually tuned to  $k_p = 1$  and  $k_i = 15000$ . The *GridState* value connected to the switches was used to make sure that for this simulation scenario the flywheel system only regulates voltage during off-grid state.



The flywheel system reacted relatively fast to the power interruption. During the disconnection from the main grid at the simulation time of 25 seconds the load block experienced a dip in the power supply for about 10 ms that fully recovered in about 20 ms, while the reconnection dip at the simulation time of 30 seconds was much shorter, about 0.5 ms.

During the islanded mode the power provided by the modeled flywheel system had a ripple of about 500 W. The harmonic content of the voltage and current experienced by the load during off-grid mode were measured to be  $THD_U = 1,52\%$  and  $THD_I = 1,58\%$  respectively.

### 3.1.2 Grid synchronization

During the islanded operation it is often difficult for the microgrid to retain its frequency due to the smaller scale (inertia) of the microgrid. It is crucial for the microgrid and the main grid to be in phase before reconnecting, as otherwise the currents appearing during the transients could damage the equipment connected to both grids.

The grid synchronization scenario was simulated by first charging up the flywheel system to about 4000 rpm. After the microgrid was disconnected from the main grid the *Programmable Voltage Source* block was instructed to introduce a  $30^\circ$  phase shift in the voltage of the main grid. Phase angles of both grids were measured using a phase locked loop (PLL). At the simulation time of 30 seconds the flywheel system started to synchronize the microgrid with the main grid by slowly adjusting the frequency of the outputted voltage. Phase measurements of the simulated synchronization of microgrid and main grid are shown in figure 3.4.

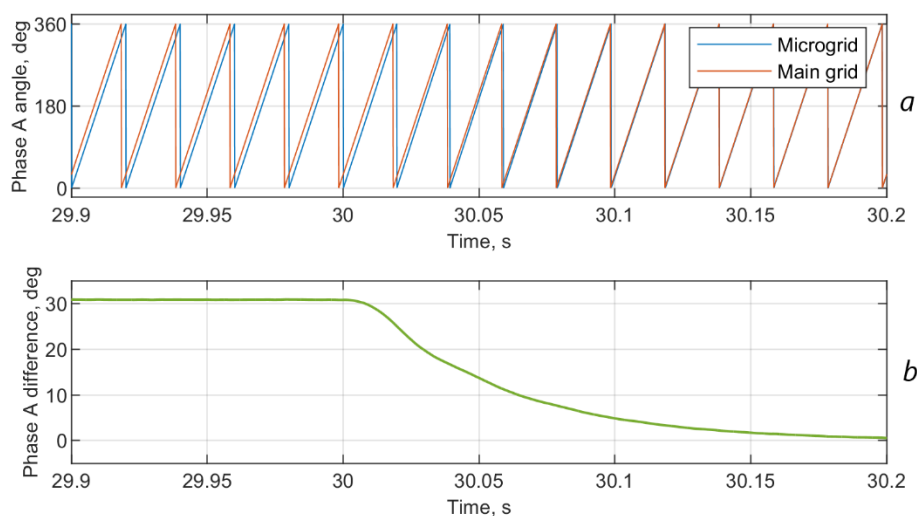


Figure 3.4 Synchronization scenario: a) phase A angles of the microgrid and main grid, b) phase A angle difference between the microgrid and main grid

The synchronization was achieved in only 0.2 seconds due to the small scale of the simulated microgrid. In real commercial systems the microgrid synchronization takes at least few minutes, as the scales are larger and there are many distributed generators that have to be controlled simultaneously usually by methods such as droop control.

## 3.2 ON-Grid Scenarios

On-grid scenarios considered in this work simulate the use of a flywheel system to regulate the grid voltage through reactive power and to perform active power load leveling.

### 3.2.1 Voltage regulation using reactive power

As discussed previously in chapter 2.2.6 that through current control the active and reactive power output of the grid-side converter can be controlled independently. The decoupled control of active and reactive power is useful from the view of power conditioning as the grid frequency can be regulated through active power and the grid voltage through reactive power.

The simulation scenario was modeled for a weak grid as the stronger the grid the more reactive power is needed to regulate the voltage. The maximum reactive power output of the modeled converter was 15 kvar. A weak microgrid was simulated by connecting with the main grid through a 20 kVA transformer.

The reactive power output of the converter was regulated by a PI controller. The necessary reactive power was evaluated by measuring the  $d$  component of the voltage and comparing it to a value of 325,3 that represents a phase-to-phase voltage of 400 V. The gains of the PI controllers were manually tuned to  $k_p = 1$  and  $k_i = 30000$ . Simulink model for reactive power control is shown in figure 3.5.

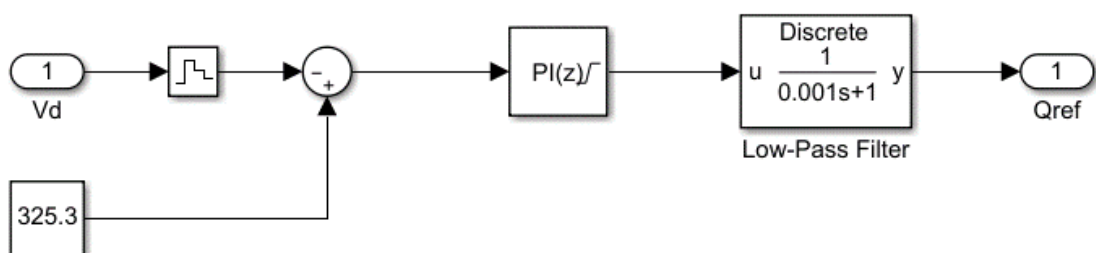


Figure 3.5 Simulink model of voltage control through reactive power

The voltage regulation capability was evaluated by reducing the voltage of the main grid by 10% from the *Programmable Voltage Source* block at the simulation time of 2 seconds. Without the support of reactive power the grid RMS voltage drops down to 207 V. However, with the reactive power support the RMS voltage was regulated back within 50 ms. The reactive power needed to regulate the voltage for this grid configuration was about -12,5 kvar, negative value here indicates that the flow of the reactive power is into grid. Voltage regulation simulations with and without reactive support are shown in figure 3.6.

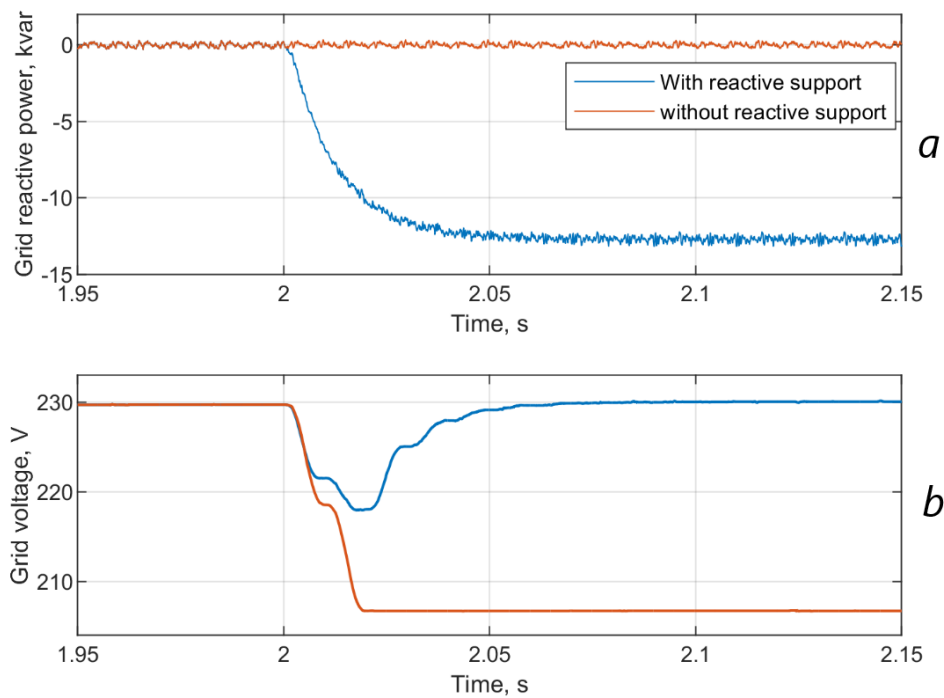


Figure 3.6 On-grid voltage regulation simulations with and without reactive support: a) grid reactive power draw, b) grid RMS voltage

### 3.2.2 Load leveling using active power

Unbalance between power production and consumption can result in fluctuations of grid voltage and frequency. Grid balancing has become an important topic, as in a modern microgrid there are many smaller distributed generators and consumers. Renewable energy sources such as wind and solar are by nature unpredictable and fluctuating, the same can also be said about consumers. As such, the purpose of this simulation was to evaluate the capabilities of the modeled flywheel energy storage system for load leveling scenario.

The Simulink block for variable load had to be created as discussed in chapter 2.1.1. The load profile was constructed from one second power measurements of the NRG building in Tallinn University of Technology. A two minute segment was used as shown in figure 3.7.

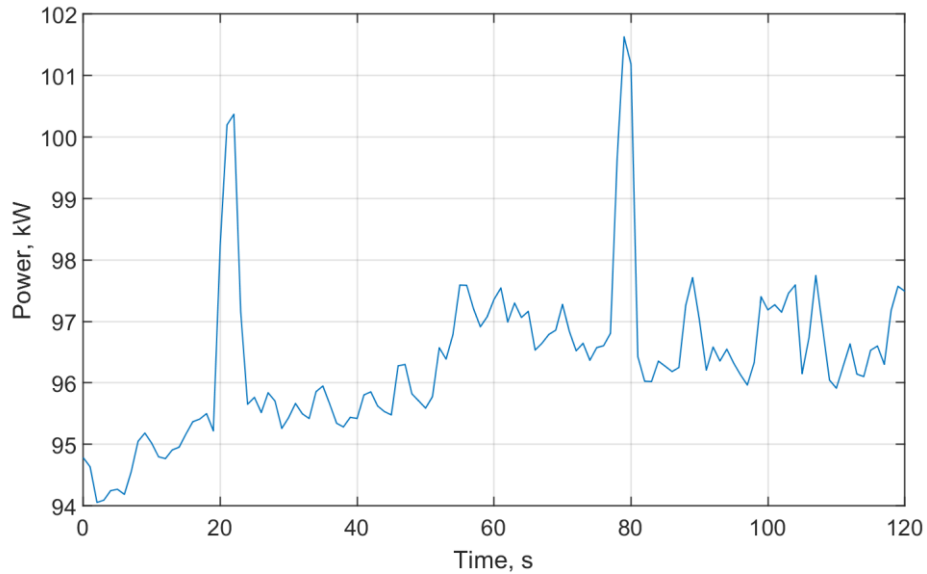


Figure 3.7 Variable load profile used for load leveling

The idea of load leveling scenario was to level the power draw from the grid by using the flywheel system to either draw or supply power as the grid power fluctuated over some average value as shown in figure 1.7 of chapter 1.3.3.

The power output of the flywheel system was established by taking a moving average of the measured power draw of the load. The window length for the moving average was set at first 30 seconds, long enough to provide good leveling, while not long enough to make the simulation time too long. The power output for the flywheel system was calculated by subtracting the moving average value from the measured power draw of the load.

Over longer duration the running losses of motor will however start slowing down the flywheel system. To alleviate this problem the power output of GSC was adjusted by a value dependent on the rotational speed of the flywheel. The trendline equation 3.1 of running losses was calculated from power draw samples of the flywheel system during standby mode at multiple different speed levels. The Simulink model for load leveling is showed in figure 3.8.

$$P_{\text{loss}} = 0,00005N^2 - 0,0468N + 195,26 \quad (3.1)$$

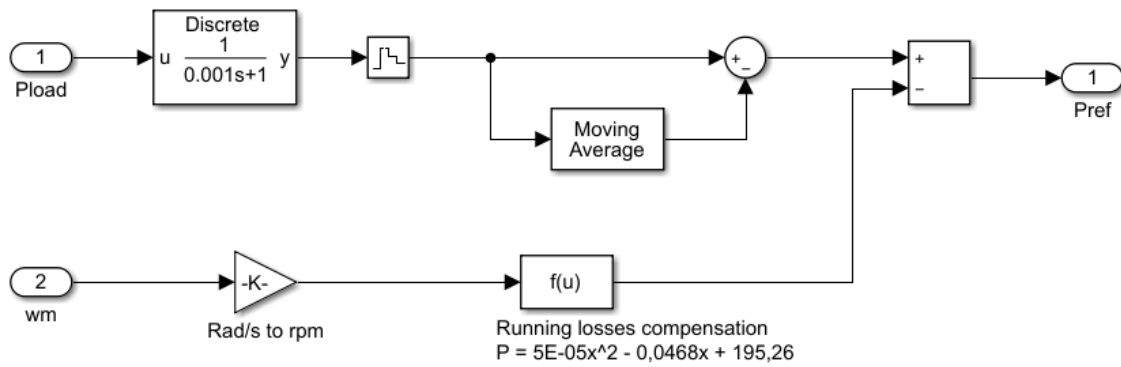


Figure 3.8 Simulink model for load leveling

Simulations with and without load leveling are shown in figure 3.9. The simulation was set up by first charging the flywheel up to about 4400 rpm. At the simulation time of 30 seconds a variable load was turned on. During the load leveling scenario the flywheel system started to even out the power draw from grid. It can be seen that the flywheel speed drops sharply to compensate the two peaks at the simulation times of 50 and 110 seconds.

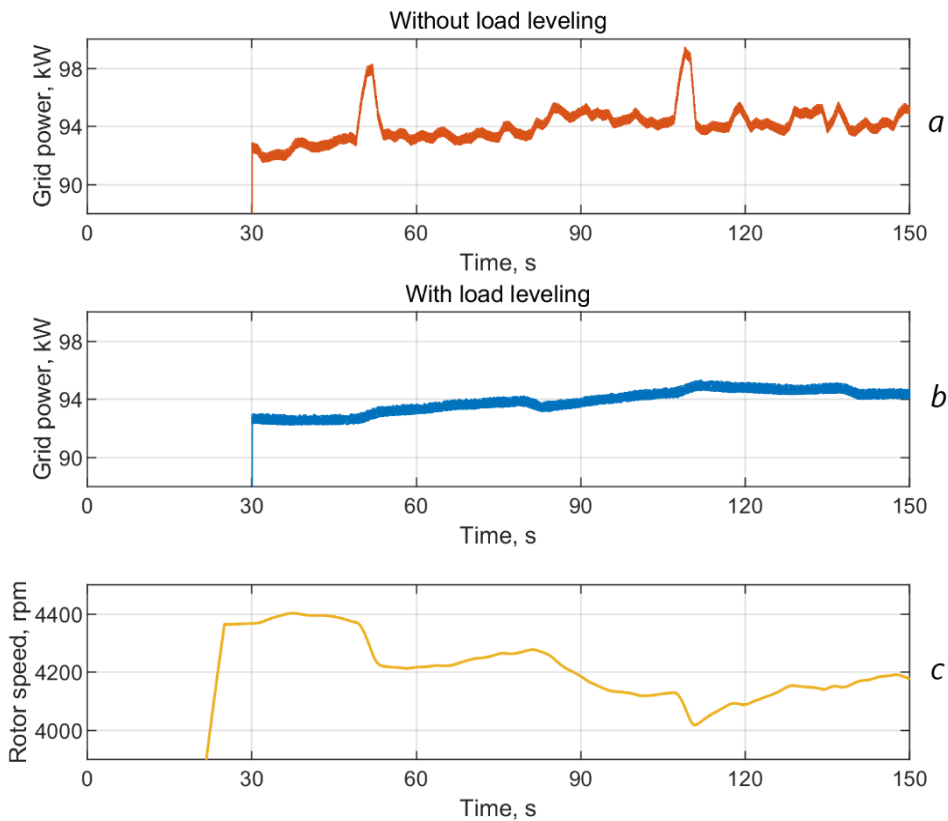


Figure 3.9 Load leveling simulation scenario: grid power draw a) without load leveling, b) with load leveling and c) flywheel rotor speed while load leveling.

The performance of load leveling was evaluated using the root mean squared error (RMSE) value, which describes the standard deviation between the regression line of the grid power draw and the actual power draw. Without load leveling the RMSE value was 1030 W, while with load leveling it was 312 W, a 69,7% drop. By increasing the window for the moving average the performance of load leveling could be increased even further. With a 60 second moving average the RMSE value was now 186 W, a 81,9% drop from no load leveling. However, with longer moving averages the flywheel system has to do more work, resulting in larger speed variations.

The flywheel system seems to successfully level the loads, however for long term leveling the flywheel might reach either its minimum or maximum rotational speed depending on the length of the moving average and the long term increasing or decreasing trend of the loads. To overcome this problem a suggestion for future research is to develop a leveling algorithm that would either be more aggressive or conservative depending on the rotor speed.

## SUMMARY

The goal of this work was to develop simplified models and control strategies for a flywheel energy storage system to improve power/voltage quality and stability in a microgrid with weak grid connection or in an islanded microgrid.

In the first part of this thesis an overview of the flywheel energy storage system was given. Comparison with other competing storage systems such as batteries and supercapacitors was drawn, explaining the position of flywheel system as high power storage with high charge cycle durability and medium capacity. From these characteristics the suitable uses for flywheel systems were defined as cyclic, high power applications such as: load leveling, voltage and frequency regulation and use as a short term uninterruptible power source.

The second part of this thesis presented the development process of the flywheel storage model. It gave an overview of the modeled physical components of the flywheel system and modeled grid and consumer load. The parameters of Rosetta T3-15 flywheel system were used as basis for the modeled flywheel system. The parameters of the LCL filter were established, with the total harmonic distortion of the output voltage and current being  $THD_U = 0,65\%$  and  $THD_I = 1,00\%$  at rated power of 15 kW. A dynamic load was modeled that used one second power measurements in the NRG building of Tallinn University of Technology as a load profile.

The control methods for both grid-side and motor-side converter were modeled - current control and field-oriented control respectively. Descriptions of the converter control during startup, standby and motoring states were given. The round-trip efficiency of the modeled flywheel was 80,2% compared to 77,6% of Rosetta T3-15 flywheel system.

In the third part of the thesis multiple different on- and off-grid scenarios were simulated. The modeled flywheel system was able to take over in 10 ms after a power failure as simulated in the islanding / uninterruptible power source scenario. A microgrid with very small inertia was successfully synchronized to a main grid shifted  $30^\circ$  in 0,2 seconds. In voltage regulation scenario a 10% drop in voltage was regulated back in 50ms using reactive power. Active power load leveling was successfully performed, with 81,9% drop in root mean squared error (RMSE) of the grid power draw fluctuations.

In conclusion, in this thesis models and control strategies of flywheel energy storage system were developed. The scenarios modeled provide insight into some of the power conditioning capabilities of the flywheel storage system. The flywheel system modeled in this thesis can be used as a base for modeling of other flywheel systems with different power, storage capabilities and as a starting

point for evaluation of investment and operational costs by determining the size of the needed flywheel system.

This work done in this thesis is planned to be used in other works that include research into:

- Combined usage of flywheel storage with other storage systems, such as battery systems, to prolong the battery lifetime, etc.
- Flywheel storage usage in nearly zero energy building microgrid models that are subject to demand response or demand side management.

Based on the work of this thesis the Rosetta T3-15 flywheel system is planned to be retrofitted to be able to perform power conditioning by making the following changes:

- Inclusion of an auxiliary power supply for the converters.
- Addition of a programmable RLC load.
- Modifications of the distribution box to accommodate for above changes.

## KOKKUVÕTE

Käesoleva lõputöö eesmärgiks oli arendada lihtsusatud mudelid ja juhtimisstrateegiad hooratas-energiasalvesti kasutuseks võimsuse ja pingekvaliteedi parendamiseks nõrga ühendusega mikrovõrgus või võrguühenduseeta mikrovõrgus.

Töö esimeses osas anti ülevaade hooratas-energiasalvestist. Toodi võrdlus konkureerivate akusüsteemide ja ülikondensaatorite salvestusseadmetega. Võrdlusest tuli välja hooratas-energiasalvestit omadus olla suure võimsuse, kõrgete laadimistsüklitega ja keskmise mahtuvusega salvesti. Nendest karakteristikutest tulenevalt on hooratas-energiasalvestit soovituslik kasutada tsükliliste, kõrge võimsusega rakendustes, nagu koormuse tasandamine, pinge või sageduse reguleerimine ja katkematu toite allikana.

Töö teises osas kirjeldati hooratas-energiasalvesti mudelite arendamise protsessi. Anti ülevaade mikrovõrgu mudeli komponentidest nagu hooratas-energiasalvestist, tarbijatest ja võrguühendusest. Hooratas-energiasalvesti modelleeriti Rosetta T3-15 süsteemi parameetrite alusel. LCL filtri komponentide väärtused arvutati, kusjuures väljundpinge ja –voolu moonutusteks olid  $THD_U = 0,65\%$  ja  $THD_I = 1,00\%$  nimivõimsusel 15 kW. Muutuva koormuse jaoks loodi eraldi mudel, selle koormusprofiiliks kasutati ühe sekundilisi võimsuse mõõtmisi Tallinna Tehnikaülikooli NRG hoones.

Võrgupoolset muundurit juhiti voolu juhtimise (*current control*) kaudu ning mootoripoolse muunduri juhtimiseks kasutati magnetvälja juhtimise (*field-oriented control*) meetodit. Muundurite juhtimist kirjeldati erinevates *startup*, *standby* ja *motoring* olekutes. Modelleeritud hooratas-energiasalvesti laadimis-mahalaadimistsükli efektiivsus oli 80,2%, võrreldes Rosetta T3-15 süsteemi 77,6% – ga.

Töö kolmandas osas simuleeriti mitmeid erinevaid võrguühendusega ja -ühenduseeta stsenaariume. Modelleeritud hooratas-energiasalvesti suutis katkematu toiteallikana võtta üle võrgutoite 10 ms jooksul peale toitekatkestust. Väga väikse inertsiiga mikrovõrk sünkroniseeriti 30° faasinihkes olnud peavõrguga 0,2 sekundi jooksul. Pinge reguleerimise stsenaariumis reguleeriti 10%-ne pingelang tagasi 50 ms jooksul kasutades reaktiivvõimsust. Aktiivvõimsuslik muutuv koormus tasandati edukalt, tuues 81,9% languse võimsuse *root mean squared error (RMSE)* võnkumises.

Kokkuvõttes, käesolevas lõputöös arendati välja hooratas-energiasalvesti ja selle juhtimise mudelid. Testitud stsenaariumid annavad ülevaate hooratas-energiasalvesti võimsuskvaliteedi parendamise võimetest. Modelleeritud hooratas-energiasalvesti mudelit saab kasutada alusena erinevate parameetritega hooratas-energiasalvestussüsteemide modelleerimiseks ning

investeermise ja tegevuskulude hindamise aluspunktina vajamineva hooratas-energiasalvesti suuruse dimensioneerimise kaudu.

Käesolevat lõputööd plaanitakse kasutada ka teistes töödes, mille uurimisvaldkondadeks on:

- Hooratas-energiasalvesti kombineeritud kasutus teiste salvestussüsteemidega nagu akusüsteemidega, aku eluea pikendamiseks, jms.
- Hooratas-energiasalvesti kasutus liginullenergiahoonetel baseeruva mikrovõrgu mudelites, kus tegeldakse tarbimise juhtimisega

Käesoleva lõputöö alusel kavatakse uuendada Rosetta T3-15 hooratas-energiasalvesti süsteemi, võimsuse kvaliteedi parendamise otstarbeks, tuues sisse olemasolevasse süsteemi järgnevad muudatused:

- Lisatoite kaasamine muundurite jaoks.
- Programmeeritava RLC koormuse lisamine.
- Elektrivarustuse ümberprojekteerimine ülalolevatest muutustest tulenevalt.

## REFERENCES

- [1] "Renewable energy directive (2009/28/EC)," [Online]. Available: <http://data.europa.eu/eli/dir/2009/28/oj>. [Accessed 18. 05. 2019].
- [2] Taastuvenergeetika, "Taastuvenergia aastaraamat 2017," 2017. [Online]. Available: <http://www.taastuvenergeetika.ee/wp-content/uploads/2018/06/Taastuvenergia-aastaraamat-2017.pdf>. [Accessed 18. 05. 2019].
- [3] "Directive 2010/31/EU of the European Parliament and of the Council of 19 May 2010 on the energy performance of buildings," [Online]. Available: <https://eur-lex.europa.eu/eli/dir/2010/31/oj>. [Accessed 17. 05. 2019].
- [4] Energiatalgud, "Mikro- ja hajatootmine," [Online]. Available: [https://energiatalgud.ee/index.php/Mikro-ja\\_hajatootmine?menu-83](https://energiatalgud.ee/index.php/Mikro-ja_hajatootmine?menu-83). [Accessed 18. 05. 2019].
- [5] M. E. Amiryar and K. R. Pullen, "A Review of Flywheel Energy Storage System Technologies and Their Applications," *Applied Sciences*, vol. 7, no. 3, p. 286, 2017.
- [6] P. Nikolaidis and A. Poullikkas, "A comparative review of electrical energy storage systems for better sustainability," *Journal of Power Technologies*, vol. 97, no. 3, pp. 220-245, 2018.
- [7] R. Peña-Alzola, R. Sebastián, J. Quesada and A. Colmenar, "Review of Flywheel based Energy Storage Systems," *IEEE*, 2011.
- [8] B. Bolund, H. Bernhoff and M. Leijon, "Flywheel energy and power storage systems," *Renewable and Sustainable Energy Reviews*, vol. 11, no. 2, pp. 235-258, 2007.
- [9] P. Yulong, A. Cavagnino, V. Silvio, C. Feng and A. Tenconi, "Flywheel energy storage systems for power systems application," in *ICCEP*, Santa Margherita Ligure, 2017.
- [10] J. Yan, *Handbook of Clean Energy Systems, volume 5 - Energy Storage*, Wiley, 2015.
- [11] E. H. E. Bayoumi, "Power electronics in smart grid distribution power systems: a review," *International Journal of Industrial Electronics and Drives*, vol. 3, no. 1, pp. 20-48, 2016.
- [12] A. Rahmoun, "Mathematical Modeling and Analysis of a Battery Energy Storage System for Microgrids," Ph.D dissertation, Department of Electrical Power Engineering and

- Mechatronics, Tallinn University of Technology, 2017. [Online]. Available: <https://digi.lib.ttu.ee/i/?9116>. [Accessed 15. 05. 2019].
- [13] B. Zohuri, *Energy Storage Technologies and Their Role in Renewable Integration*, Springer, Cham, 2018.
- [14] M. Hedlund, J. Lundin, J. d. Santiago, J. Abrahamsson and H. Bernhoff, "Flywheel Energy Storage for Automotive Applications," *Energies*, vol. 8, no. 10, pp. 10636-10663, 2015.
- [15] A. K. Arania, H. Karami, G. Gharehpetian and M. Hejazi, "Review of Flywheel Energy Storage Systems structures and applications in power systems and microgrids," *Renewable and Sustainable Energy Reviews*, vol. 69, pp. 9-18, 2017.
- [16] A. Ali, W. Li, R. Hussain, X. He, B. W. Williams and A. H. Memon, "Overview of Current Microgrid Policies, Incentives and Barriers in the European Union, United States and China," *Sustainability*, vol. 9, no. 7, pp. 1-28, 2017.
- [17] M. A. Dan T.Ton, "The U.S. Department of Energy's Microgrid Initiative," *The Electricity Journal*, vol. 25, no. 8, pp. 84-94, 2012.
- [18] Solar Power Events, "Smart energy microgrid marketplace," [Online]. Available: <https://events.solar/midwest/smart-energy-microgrid-marketplace/>. [Accessed 07. 05. 2019].
- [19] MathWorks, "Retune the Drive Parameters," [Online]. Available: <https://www.mathworks.com/help/physmod/sps/powersys/ug/advanced-users-retune-the-drive-parameters.html>. [Accessed 30. 04. 2019].
- [20] A. Reznik, M. G. Simões, A. Al-Durra and S. M. Mueeen, "LCL Filter Design and Performance Analysis for Grid-Interconnected Systems," *IEEE Transactions on Industry Applications*, vol. 50, no. 2, pp. 1225 - 1232, 2013.
- [21] S.-H. Kim, *Electric Motor Control*, Amsterdam: Elsevier, 2017.
- [22] B. K. Bose, *Modern Power Electronics and AC Drives*, New Jersey: Prentice-Hall, 2002.
- [23] STMicroelectronics, "Sensor field oriented control (IFOC) of three-phase AC induction motors using ST10F276," 2006. [Online]. Available: [https://www.st.com/content/ccc/resource/technical/document/application\\_note/06/30/4](https://www.st.com/content/ccc/resource/technical/document/application_note/06/30/4)

a/f2/c8/e3/48/e5/CD00116774.pdf/files/CD00116774.pdf/jcr:content/translations/en.CD00116774.pdf. [Accessed 14 05 2019].

- [24] Y. Solbakken, "Vector control for dummies," Switchcraft, 2017. [Online]. Available: <https://www.switchcraft.org/learning/2016/12/16/vector-control-for-dummies>. [Accessed 10. 04. 2019].
- [25] N. P. Quang and J.-A. Dittrich, Vector Control of Three-Phase AC Machines - System Development in the Practice, Berlin: Springer, 208.
- [26] A. Hirofumi, H. W. Edson and A. Mauricio, Instantaneous Power Theory and Applications to Power Conditioning, New Jersey: Wiley, 2007.
- [27] T. Fitzermann, "PMSM (Permanent magnet synchronous motor) control simulation," [Online]. Available: <http://www.sosw.poznan.pl/tfitzer/pmsm/>. [Accessed 10. 04. 2019].
- [28] MathWorks, "Clarke Transform," [Online]. Available: [https://www.mathworks.com/help/phymod/sps/ref/clarketransform.html?s\\_tid=srchtitle](https://www.mathworks.com/help/phymod/sps/ref/clarketransform.html?s_tid=srchtitle). [Accessed 10. 04. 2019].
- [29] MathWorks, "Park Transform," [Online]. Available: [https://www.mathworks.com/help/phymod/sps/ref/parktransform.html?s\\_tid=srchtitle](https://www.mathworks.com/help/phymod/sps/ref/parktransform.html?s_tid=srchtitle). [Accessed 10. 04. 2019].
- [30] Electrical4U, "Field Oriented Control," [Online]. Available: <https://www.electrical4u.com/field-oriented-control/>. [Accessed 25. 04. 2019].
- [31] MathWorks, "Simulate an AC Motor Drive," [Online]. Available: <https://www.mathworks.com/help/phymod/sps/powersys/ug/simulating-an-ac-motor-drive.html#f4-7692>. [Accessed 26. 04. 2019].
- [32] H. v. d. Broeck, H.-C. Skudelny and G.V.Stanke, "Analysis and realization of a pulsewidth modulator based on voltage space vectors," *IEEE Transactions on Industry Applications*, vol. 24, no. 1, pp. 142-150, 1988.
- [33] J.G.D.Oliveira, "Power Control Systems in a Flywheel based All-Electric Driveline," Ph.D dissertation, Department of Engineering Sciences, Uppsala University, 2011. [Online]. Available: <https://uu.diva-portal.org/smash/get/diva2:434755/FULLTEXT01.pdf>. [Accessed 03. 04. 2019].

- [34] Y. Solbakken, "Space Vector PWM Intro," Switchcraft, 2017. [Online]. Available: <https://www.switchcraft.org/learning/2017/3/15/space-vector-pwm-intro>. [Accessed 03. 04. 2019].
- [35] C. Techniques, "Unidrive SP User Guide," *Unidrive 2403 Datasheet*, May 2008.
- [36] MathWorks, "Space Vector Modulator," [Online]. Available: [https://www.mathworks.com/help/physmod/sps/powersys/ref/spacevectormodulator.html?s\\_tid=srchtitle](https://www.mathworks.com/help/physmod/sps/powersys/ref/spacevectormodulator.html?s_tid=srchtitle). [Accessed 08. 04. 2019].
- [37] Q.-C. Zhong and T. Hornik, *Control of Power Inverters in Renewable Energy and Smart Grid Integration*, Wiley-IEEE Press, 2013.
- [38] T. Kalitjuka, "Control of Voltage Source Converters for Power System Applications," M.S. Thesis, Department of Electric Power Engineering, Norwegian University of Science and Technology, 2011.

## APPENDICES

Appendix 1 Matlab code used for flywheel system modeling .....	70
Appendix 2 Simulink model of physical components .....	72
Appendix 3 Simulink model of variable load block .....	73
Appendix 4 Simulink model of FESS control.....	74
Appendix 5 Simulink model of state selection logic.....	75
Appendix 6 Simulink model of startup mode.....	76
Appendix 7 Simulink model of motorin/regen mode .....	77
Appendix 8 Simulink model of standby mode .....	78
Appendix 9 Simulink model of Speed Controller .....	79
Appendix 10 Simulink model of Field-Oriented Control of MSC.....	80
Appendix 11 Simulink model of Current Control of GSC.....	81

## Appendix 1 Matlab code used for flywheel system modeling

```

Ts = 5e-6;           % fundamental timestep, s
Tsc = 20e-6;        % speed control timestep
Tvect = 20e-6;      % vector control timestep
Treg = 20e-6;       % sim scenario timestep

% LCL filter parameter calculations
% System parameters
En = 400;           % Grid voltage ph-ph
P = 15e3;           % Inverter Power rating
Vdc = 700;          % DC-Link voltage
w = 2*pi*50;        % Grid frequency, rad/s
fsw = 16e3;         % Switching frequency, Hz
x = 0.01;           % Max power factor variation, 1%
rip = 0.02;         % Max current ripple, 2%

% Base values
Zb = En^2/P;
Cb = 1/(Zb*2*pi*50);

%Filter paramaters
%{
Cf = x*Cb           % Filter capacitor, C
Iripple = rip*(P*sqrt(2))/(3*120); % Max current ripple, A
Li = Vdc/(6*fsw*Iripple) % Inverter-side inductor
Lg = (sqrt(1/0.2^2)+1)/((0.01*Cb)*(2*pi*fsw)^2) % Grid-side inductor, F
f0 = (1/(2*pi))*sqrt((Li+Lg)/(Li*Cf*Lg)); % Cut-off frequency, Hz
Rd = 1/(3*2*pi*f0*Cf) % Damping resistor, Ohm
%}

% Rounded values for the filter
Cf = 3e-6; % 3 uF
Li = 0.0062; % 6.2 mH
Lg = 2e-4; % 0.2 mH
Rd = 2.7; % 2.7 Ohm

% Gains of Current control of Grid-side converter
kp_cc = 30;
ki_cc = 100;

%% Asynchronous Machine
Pn = 15e3;
Vn = 400;
fn = 50;
Rs = 0.2147; % stator resistance
Lls = 0.001991; % stator leakage inductance
Rr = 0.2205; % rotor resistance
Llr = 0.001991; % rotor leakage inductance
Lm = 0.06419; % mutual inductance
Lr = Llr+Lm; % rotor inductance
Ls = Lls+Lm; % stator inductance
J = 0.102 + 2.06; % motor + flywheel inertia
Friction = 0.004; % friction coefficient
p = 1; % pole pairs

```

```

%% Motor side converter

fc_bus = 50; % dc-link voltage filter cutoff frequency

% Speed control
kp_sc = 20; % gains of speed
ki_sc = 0.09;
Tmax = 60; % max torque
Tmin = -60; % min torque

% Flux controller
kp_fc = 40; % gains of flux controller
ki_fc = 32;
freqc_fc = 16; % flux filter cutoff frequency
fluxmax = 2; % maximum flux
fluxmin = -2; % minimum flux
in_flux = 1.2; % motor initiating flux
nf = 1.2; % nominal flux

% d-axis current regulator gains
kp_Id = 50;
ki_Id = 1000;

% q-axis current regulator gains
kp_Iq = 50;
ki_Iq = 1000;

```

## Appendix 2 Simulink model of physical components

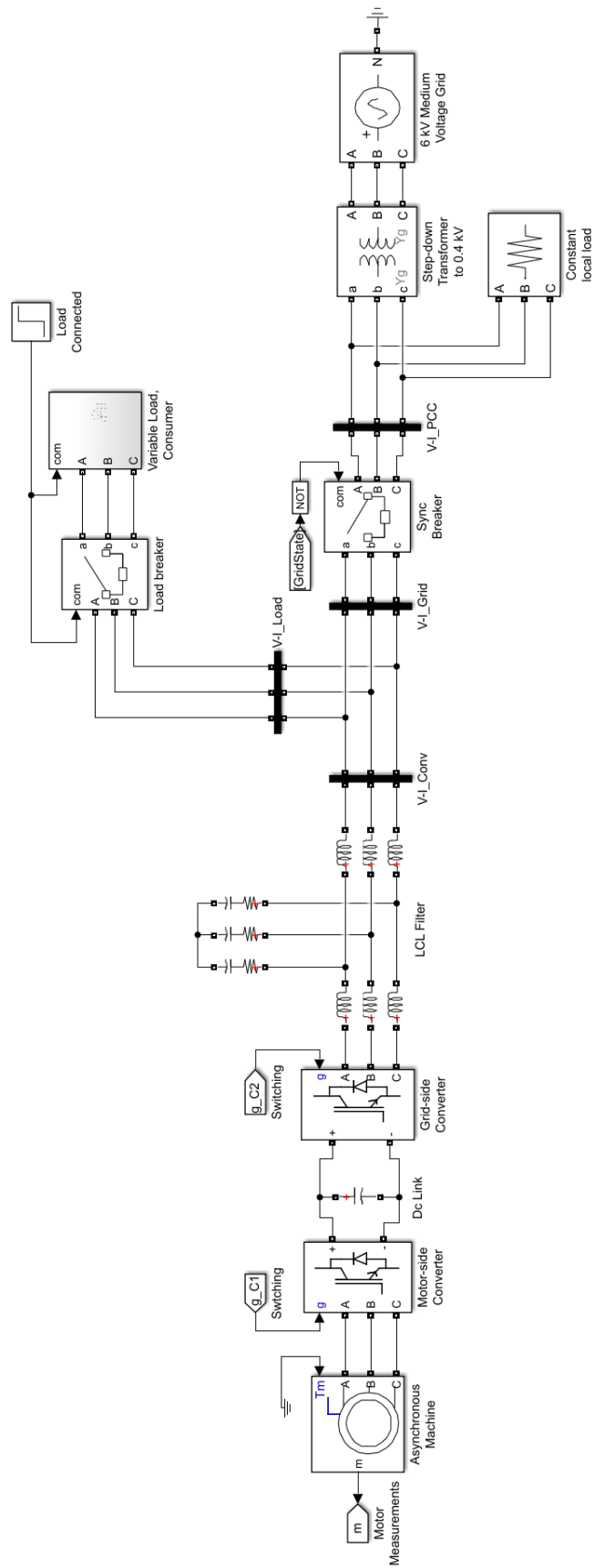


Figure A2.1 Simulink model of physical components

### Appendix 3 Simulink model of variable load block

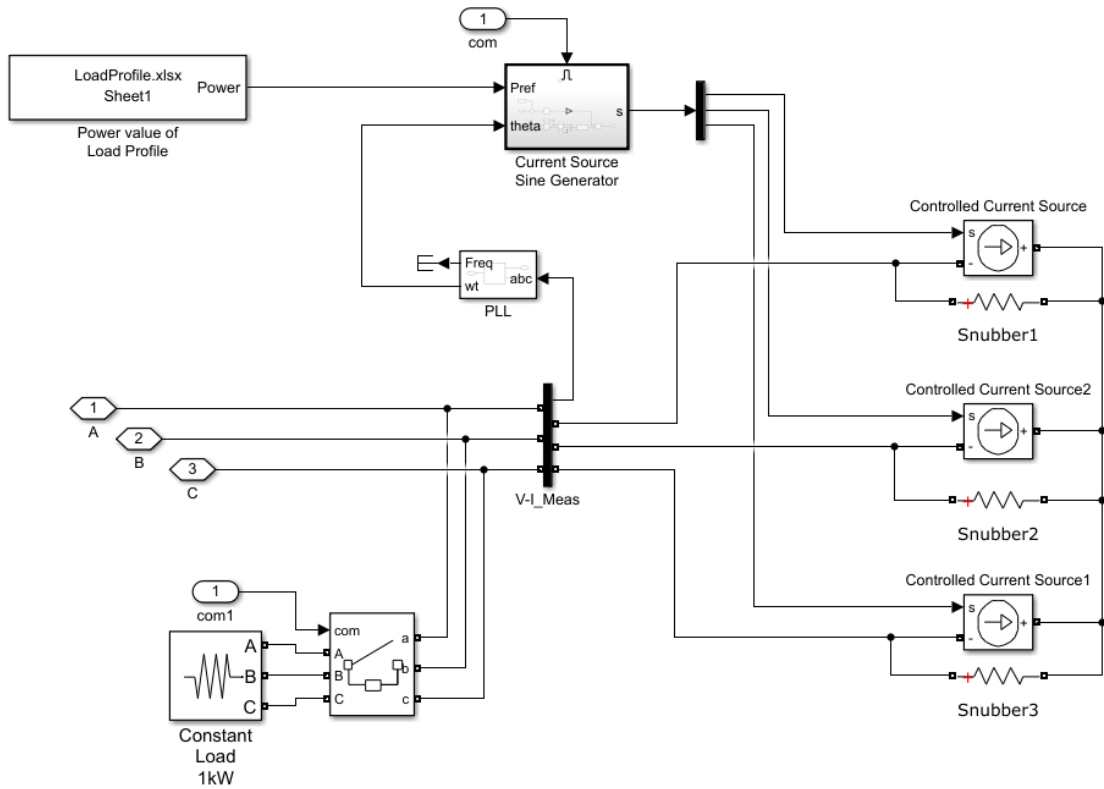


Figure A3.1 Simulink model of variable load block

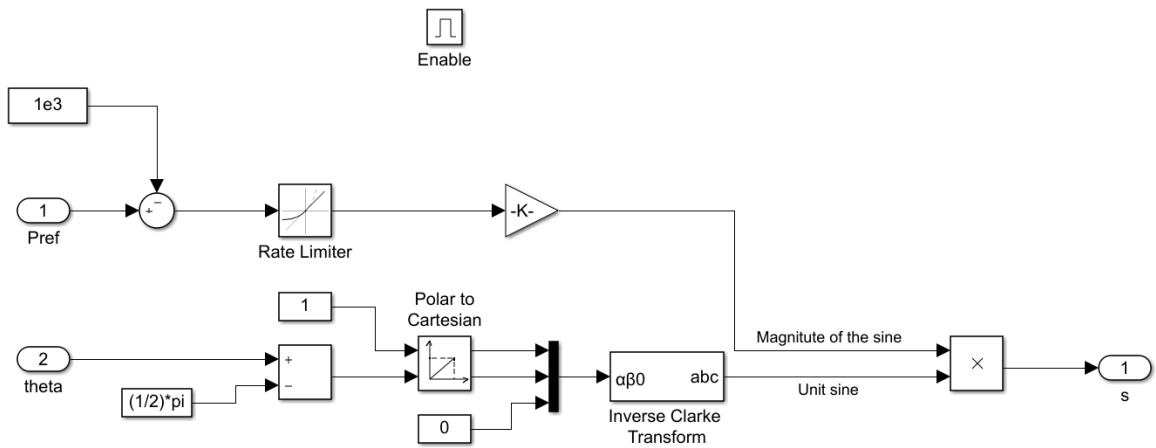


Figure A3.2 Contents of *Current Source Sine Generator* block

### Appendix 4 Simulink model of FESS control

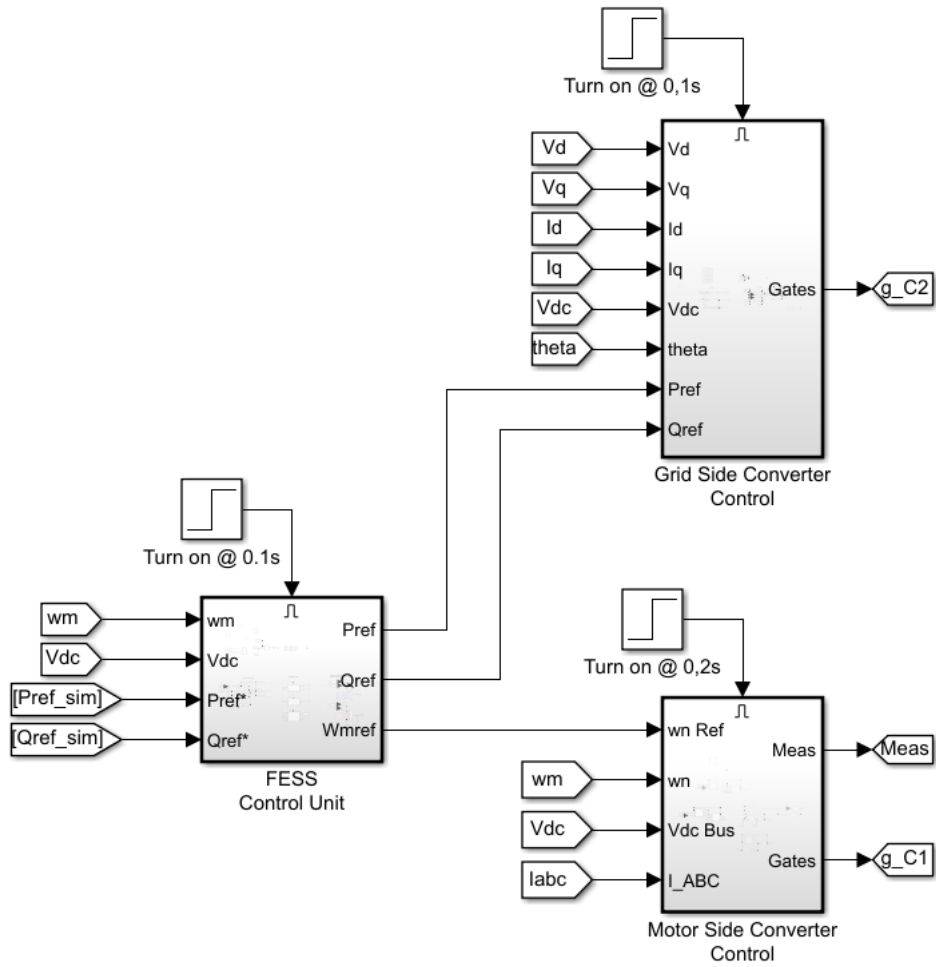


Figure A4.1 Simulink model of FESS control

## Appendix 5 Simulink model of state selection logic

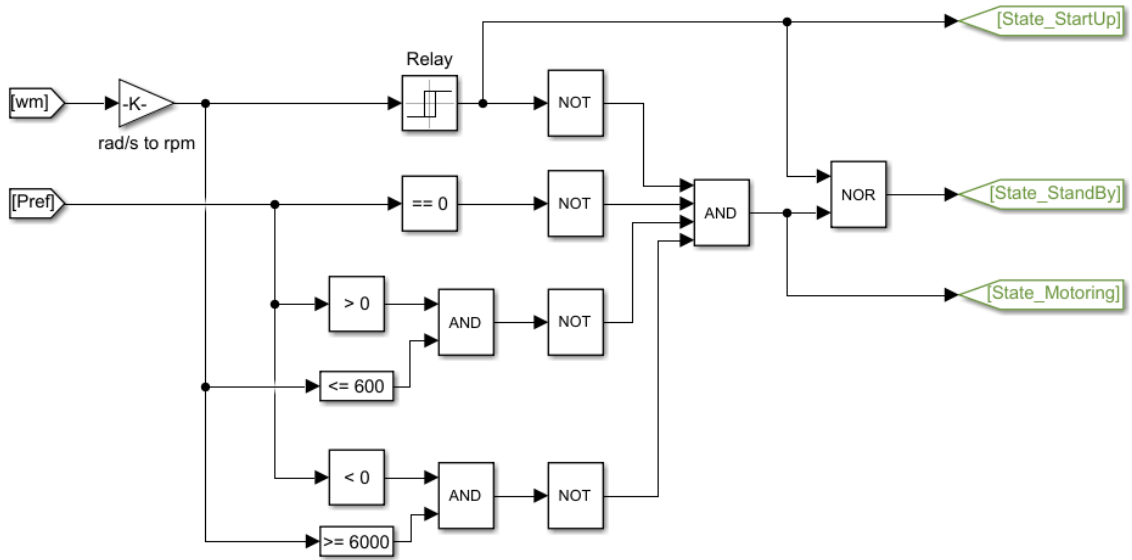


Figure A5.1 Simulink model of state selection logic

## Appendix 6 Simulink model of startup mode

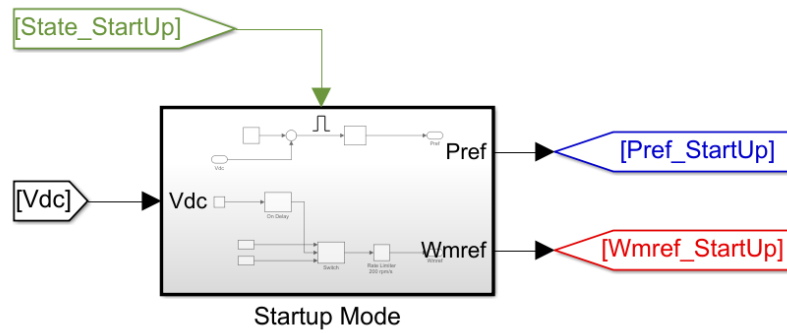


Figure A6.1 Subsystem of startup mode

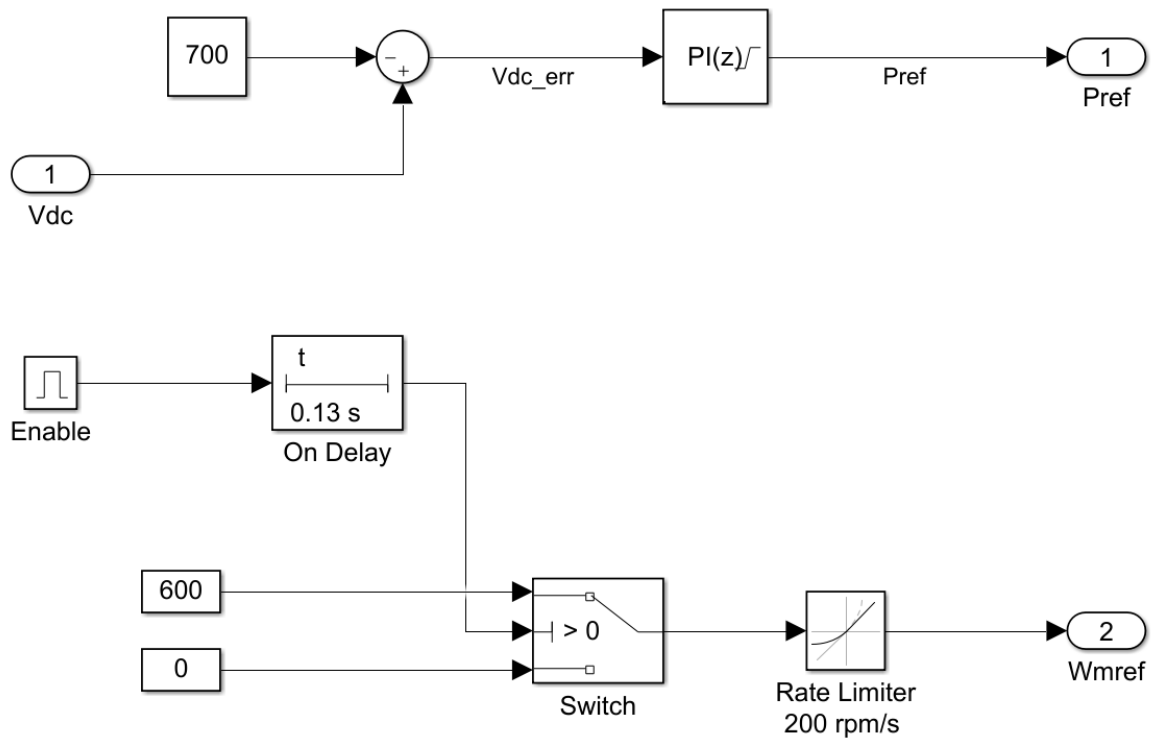


Figure A6.2 Contents of startup mode model

## Appendix 7 Simulink model of motorin/regen mode

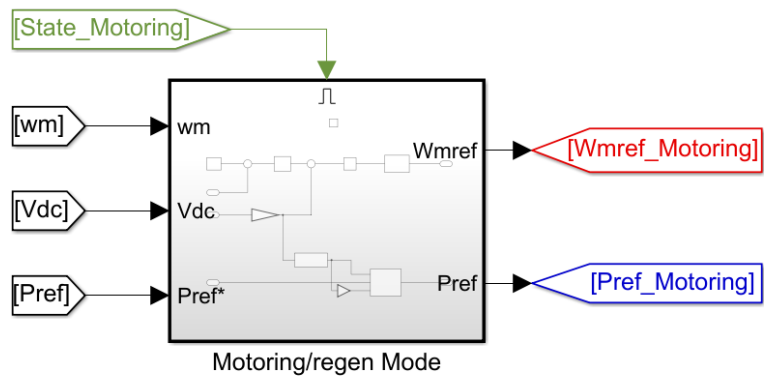


Figure A7.1 Subsystem of motoring/regen mode

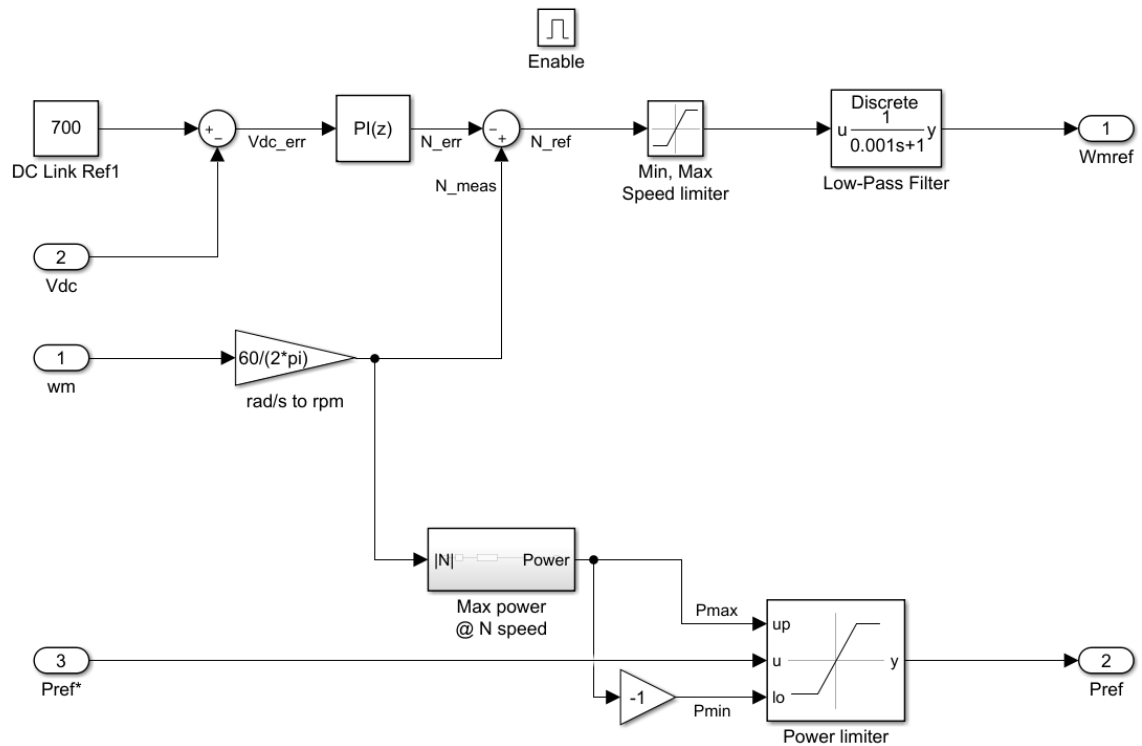


Figure A7.1 Contents of motoring/regen mode model

## Appendix 8 Simulink model of standby mode

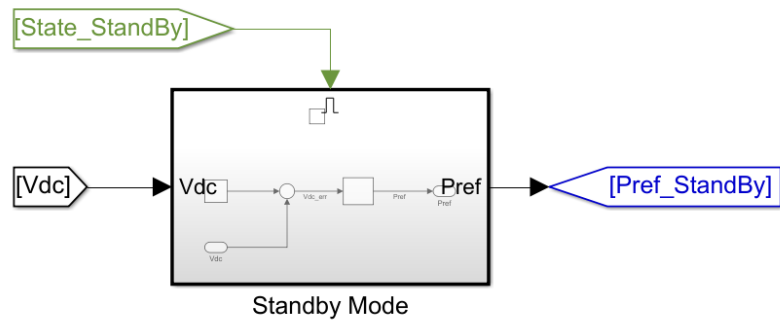


Figure A8.1 Subsystem of standby mode

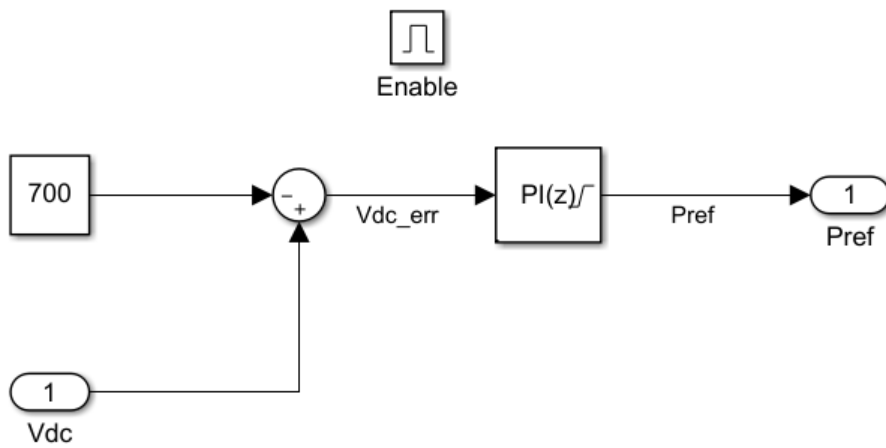


Figure A8.2 Contents of standby mode model

## Appendix 9 Simulink model of Speed Controller

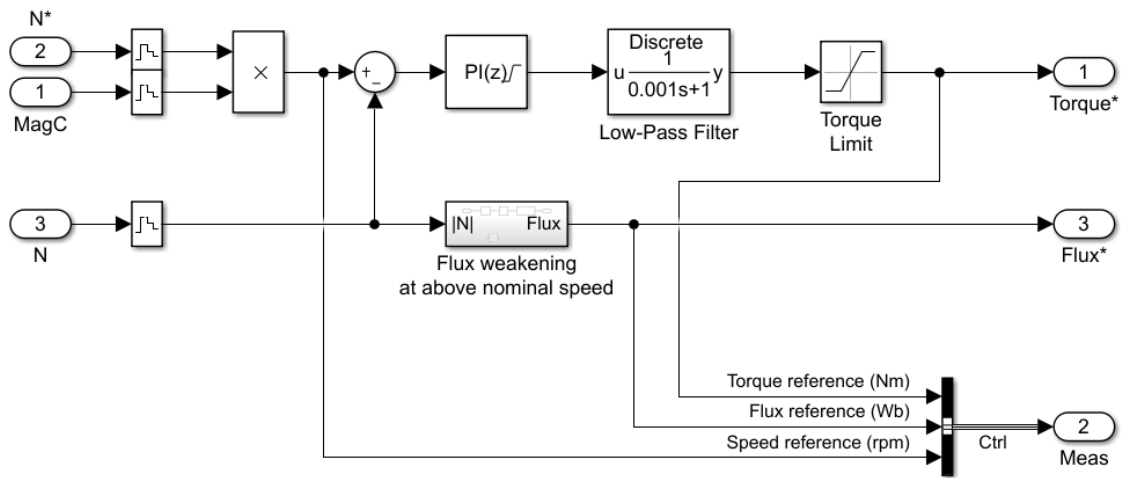


Figure A9.1 Simulink model of Speed Controller

## Appendix 10 Simulink model of Field-Oriented Control of MSC

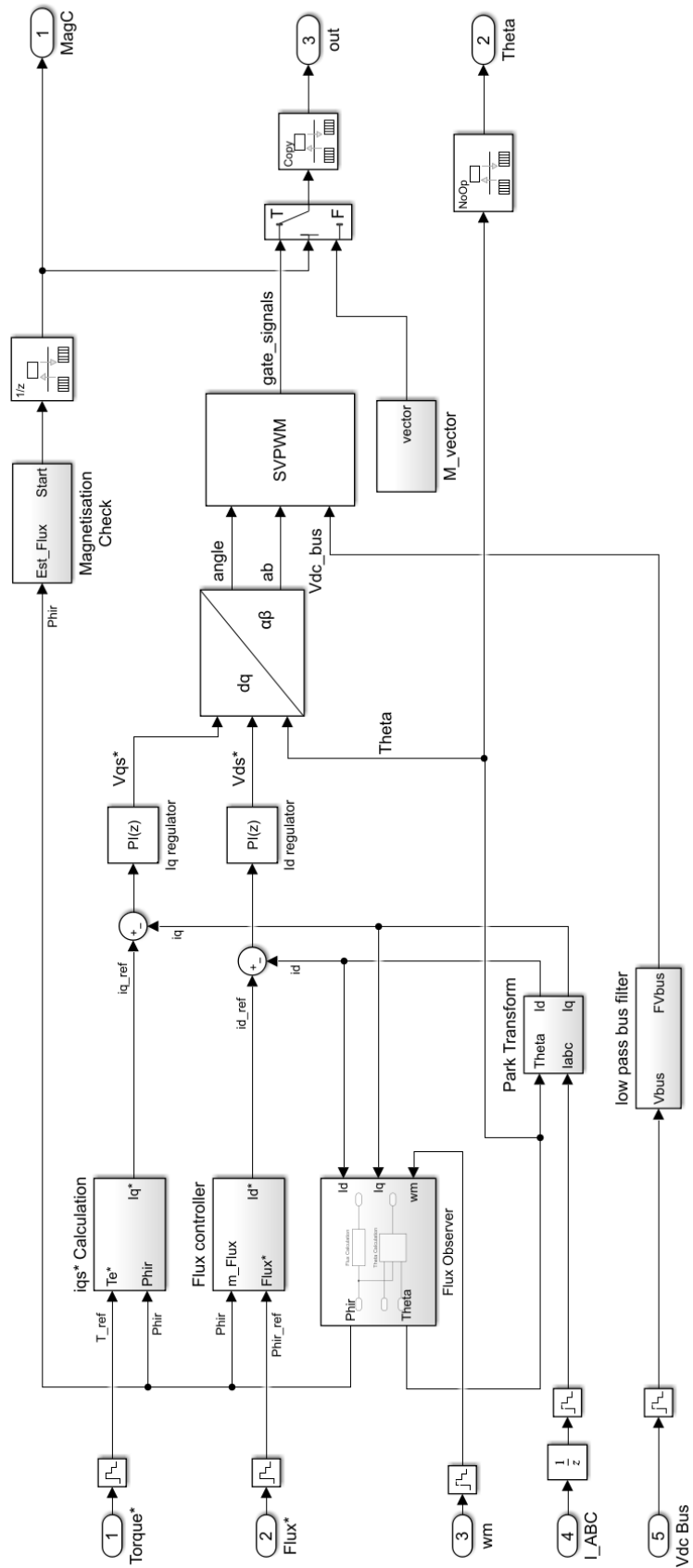


Figure A10.1 Simulink model of Field-Oriented Control of MSC

## Appendix 11 Simulink model of Current Control of GSC

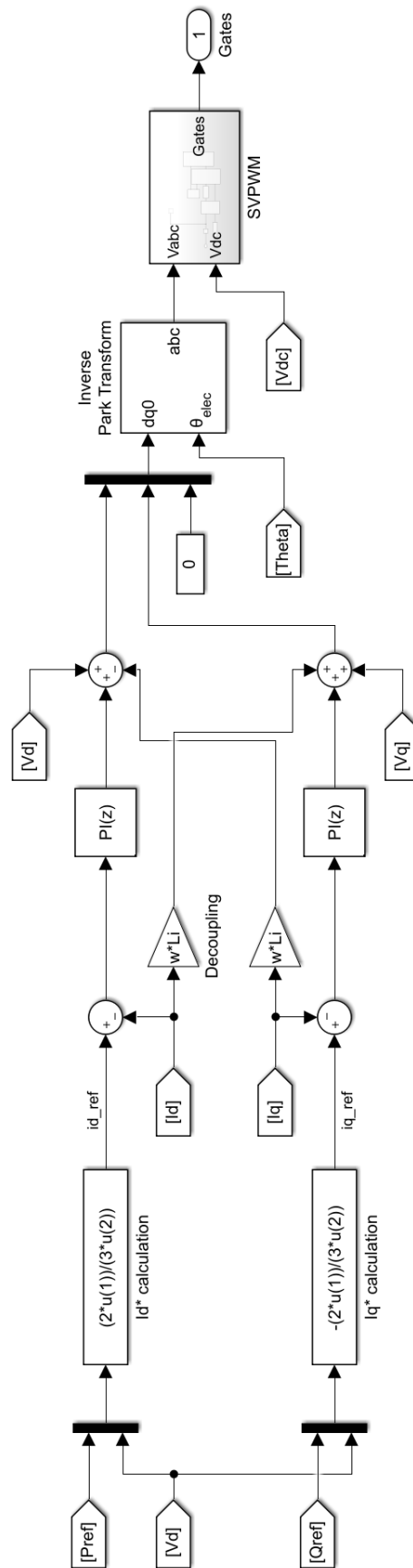


Figure A11.1 Simulink model of Current Control of GSC